Icarus 313 (2018) 61–78

Contents lists available at ScienceDirect

Icarus

journal homepage: www.elsevier.com/locate/icarus

# A new ab initio equation of state of hcp-Fe and its implication on the interior structure and mass-radius relations of rocky super-Earths

Kaustubh Hakim[a,b,*], Attilio Rivoldini[c], Tim Van Hoolst[c,d], Stefaan Cottenier[e,f], Jan Jaeken[f], Thomas Chust[g], Gerd Steinle-Neumann[g]

[a] Anton Pannekoek Institute for Astronomy, University of Amsterdam, Science Park 904, 1098XH Amsterdam, The Netherlands
[b] Department of Earth Sciences, Vrije Universiteit, De Boelelaan 1085, 1081HV Amsterdam, The Netherlands
[c] Royal Observatory of Belgium, Avenue Circulaire 3, 1180 Brussels, Belgium
[d] Institute of Astronomy, KU Leuven, Celestijnenlaan 200D, 3001 Leuven, Belgium
[e] Department of Electrical Energy, Metals, Mechanical Constructions and Systems, Ghent University, Tech Lane Ghent Science Park-Campus A, Technologiepark 903, 9052 Zwijnaarde, Belgium
[f] Center for Molecular Modeling, Ghent University, Tech Lane Ghent Science Park-Campus A, Technologiepark 903, 9052 Zwijnaarde, Belgium
[g] Bayerisches Geoinstitut, Universität Bayreuth, 95440 Bayreuth, Germany

ARTICLE INFO

*Article history:*
Received 2 August 2017
Revised 6 April 2018
Accepted 9 May 2018
Available online 25 May 2018

*Keywords:*
Super-Earths
Interior structure
Exoplanets
Equation of state of iron
Mass-radius relations

ABSTRACT

More than a third of all exoplanets can be classified as super-Earths based on radius (1–2 $R_\oplus$) and mass (<10 $M_\oplus$). Here we model mass-radius relations based on silicate mantle and iron core equations of state to infer to first order the structure and composition range of rocky super-Earths assuming insignificant gas envelopes. As their core pressures exceed those in the Earth by an order of magnitude, significant extrapolations of equations of state for iron are required. We develop a new equation of state of hexagonal close packed (hcp) iron for super-Earth conditions (SEOS) based on density functional theory results for pressures up to 137 TPa. A comparison of SEOS and extrapolated equations of state for iron from the literature reveals differences in density of up to 4% at 1 TPa and up to 20% at 10 TPa. Such density differences significantly affect mass-radius relations. On mass, the effect is as large as 10% for Earth-like super-Earths (core radius fraction of 0.5) and 20% for Mercury-like super-Earths (core radius fraction of 0.8). We also quantify the effects of other modeling assumptions such as temperature and composition by considering extreme cases. We find that the effect of temperature on mass (<5%) is smaller than that resulting from the extrapolation of the equations of state of iron, and lower mantle temperatures are too low to allow for rock and iron miscibility for $R$ <1.75 $R_\oplus$. Our end-member cases of core and mantle compositions create a spread in mass-radius curves reaching more than 50% in terms of mass for a given planetary radius, implying that modeling uncertainties dominate over observational uncertainties for many observed super-Earths. We illustrate these uncertainties explicitly for Kepler-36b with well-constrained mass and radius. Assuming a core composition of 0.8$\rho$ Fe (equivalent to 50 mol% S) instead of pure Fe leads to an increase of the core radius fraction from 0.53 to 0.64. Using a mantle composition of $Mg_{0.5}Fe_{0.5}SiO_3$ instead of $MgSiO_3$ leads to a decrease of the core radius fraction to 0.33. Effects of thermal structure and the choice of equation of state for the core material on the core radius of Kepler-36b are small but non-negligible, reaching 2% and 5%, respectively.



## 1. Introduction

With the discoveries of CoRoT-7b and Kepler-10b by ESA/CNES's and NASA's space telescopes, a new class of exoplanets known as super-Earths was introduced (Léger et al., 2009; Batalha et al., 2011). Borucki et al. (2011) classified super-Earths as rocky-type exoplanets in the size range 1.25–2 $R_\oplus$ without a H/He envelope. Observational studies suggest an upper cut-off radius of super-Earths at around 1.5–1.7 $R_\oplus$ (e.g., Weiss and Marcy, 2014; Buchhave et al., 2014; Rogers, 2015). The low occurrence rate of close-in (orbital period <100 d) planets between 1.5–2 $R_\oplus$ introduces a radius gap in this size range, suggesting two distinct classes of exoplanets, super-Earths and sub-Neptunes (Fulton et al., 2017). This radius gap further supports an upper limit on the size of super-Earths. About a third of the four thousand[1] exoplanets known to this day

* Corresponding author.
*E-mail address:* hakim.kaustubh@gmail.com (K. Hakim).

[1] http://exoplanetarchive.ipac.caltech.edu .

https://doi.org/10.1016/j.icarus.2018.05.005
0019-1035/

have a radius between 1–2 $R_\oplus$ or a mass of less than 10 $M_\oplus$ and can potentially be classified as super-Earths.

Mass and radius, which are the only observable properties for most super-Earths, are used to infer internal structure as well as surface and internal dynamics of exoplanets (e.g., Valencia et al., 2006; Seager et al., 2007; Wagner et al., 2011). In such studies, the mass-radius relations of solid exoplanets are computed based on assumptions about structure, composition and equation of state. The equations of state used in these studies are usually obtained by fitting material properties measured or computed at pressures of the Earth (<300 GPa). Since the central pressure of a super-Earth with 10 $M_\oplus$ is ~4 TPa (Wagner et al., 2011), the application of these equations of state require extrapolations into pressure domains where the predicted material properties are not reliable and their usage can introduce significant errors on the interior properties of super-Earths (Wagner et al., 2011). Consequently, such errors would produce uncertainties in mass-radius relations, the extent of which has not been studied previously. Due to the scarcity in experimental data and knowledge of the stability of iron at pressures beyond those in center of the Earth (Grasset et al., 2009), the choice of an appropriate equation of state of iron for modeling the interior structure of super-Earths is non-trivial. With the help of Density Functional Theory (DFT), it becomes possible to reliably determine the equation of state and stability of a material phase at such high pressures beyond experimental limits (e.g., Stixrude, 2014).

In this study, we assess the importance of various sources of uncertainty related to the equation of state of iron, to unknown core and mantle compositions and temperature in mass-radius relations of super-Earths. We assume a rocky composition for super-Earths, i.e., silicate minerals in the mantle and iron alloys in the core; we ignore water, ices or atmospheres. Our composition and structural modeling framework is given in Section 2. For mantle mineralogy, we apply a self-consistent approach to thermodynamics. In Section 3, we develop a new equation of state of iron based on ab initio calculations within DFT at pressures relevant to the core of super-Earths and compare it with other equations of state from the literature. In Section 4, we demonstrate the effects of using extrapolations of equations of state of iron on mass-radius relations of super-Earths. We quantify the effects of temperature and core and mantle composition in Section 5. Observed super-Earths are plotted in a mass-radius diagram in order to illustrate the extent of uncertainties in determining their structure and composition. As an example, we quantify the effects of the choice of a equation of state of iron, temperature, core and mantle composition on the interior structure of Kepler-36b, a super-Earth with well-constrained mass and radius, in Section 6.

## 2. Modeling of interior structure and composition

### 2.1. Structure

Structural modeling of a planet requires the computation of thermoelastic properties that depend on pressure $P$ and temperature $T$. We assume a fully differentiated planetary interior having two concentric spherical shells, mantle and core, with homogeneous chemical composition. Super-Earths might not all be differentiated due to miscibility of iron and silicates at very high temperatures as suggested by Wahl and Militzer (2015), and we will briefly discuss that possibility in Section 5.1, but focus on the interpretation of mass and radius in terms of a differentiated interior structure. The shells in our models are considered to be spherically symmetric and isotropic such that the material properties depend only on radius $r$. To compute the planetary mass, we integrate the equation describing the hydrostatic equilibrium and Poisson's equation from the center to the surface (with radius $R$). The equations are written as:

$$\frac{dP}{dr} = -\rho g, \tag{1}$$

$$\frac{dg}{dr} = 4\pi G\rho - 2\frac{g}{r}, \tag{2}$$

where $g$ is gravity, $G$ is the gravitational constant and the density $\rho(P, T)$ is calculated using an equation of state as described below. The planet's mass is then: $M = R^2 g(R)/G$.

The heat transport mechanism in the mantle is mainly controlled by viscosity, thermal conductivity and thermal expansivity (e.g., Schubert et al., 2001). Since both viscosity and conductivity increase and expansivity decreases with pressure, it is expected that the vigor of convection decreases with depth. Whether the mantle of super-Earths is convecting as a whole or only partially is still debated as relevant transport and thermoeleastic properties are not known. However, parameterized thermal (Stamenković et al., 2012; Wagner et al., 2012) and 2d numerical convection (Tackley et al., 2013) studies, using plausible assumptions about the pressure dependence of material properties, suggest that the deep mantle of large super-Earths is convecting but with a depth-increasing sluggishness, implying a super-heated lower mantle with a strong super-adiabatic thermal gradient. For our modeling we will either assume an isentrope in the whole mantle or a temperature profile that follows an isentrope in the upper mantle and a super-adiabatic gradient in the lower mantle. Since there are indications for a strong increase of the viscosity of post-perovskite (ppv) with pressure (Tackley et al., 2013), we pin the transition to the super-adiabatic temperature at the depth of the transition to ppv. The effect of these assumptions on the mass-radius relation will be discussed in Section 5.1. A vigorously convective layer is essentially isentropic and the gradient of the temperature is then given by

$$\frac{dT}{dP} = \frac{\gamma}{K_S}T, \tag{3}$$

where $\gamma$ is the Grüneisen parameter and $K_S$ is the adiabatic bulk modulus. For a given potential temperature, we compute the temperature in the mantle either by solving Eq. (3) or by computing a path of constant-entropy associated with the mantle's composition directly (see below). The thickness of the lithosphere is neglected and we use the footing temperature of the isentrope (1650 K) as the surface temperature $T_S$.

As can be seen in Fig. 1, the melting temperature of $MgSiO_3$ (Belonoshko et al., 2005) is much higher than the isentropic temperature of the mantle for pure $MgSiO_3$ at all pressures. This simple comparison suggests that the mantles of super-Earths are likely to be solid, although higher core temperatures might imply molten lower mantles. A strong viscosity increase in the lower mantle due to high pressure and the presence of ppv may inhibit convection. Less efficient cooling of the core and lower mantle may then lead to higher temperatures. Nevertheless, our calculations assume a solid mantle.

The thermal state of the core is mainly determined by the heat flow from the core to the mantle and thus depends on the capacity of the mantle to cool. If the heat flow out of the core is larger than what can be conducted along an adiabat, the whole core is convecting; if it is smaller, the core is at least partially thermally stratified. The extent of the stratified layer is mainly controlled by internal energy sources of the core (e.g., latent heat and chemical energy) that depend on poorly constrained material properties, on the composition of the core, and on its cooling rate. For this reason, we consider two end-member cases: a core convecting as a whole and an isothermal core.

At the core-mantle boundary (CMB), we consider two extreme scenarios for core temperature. In the first case, we as-

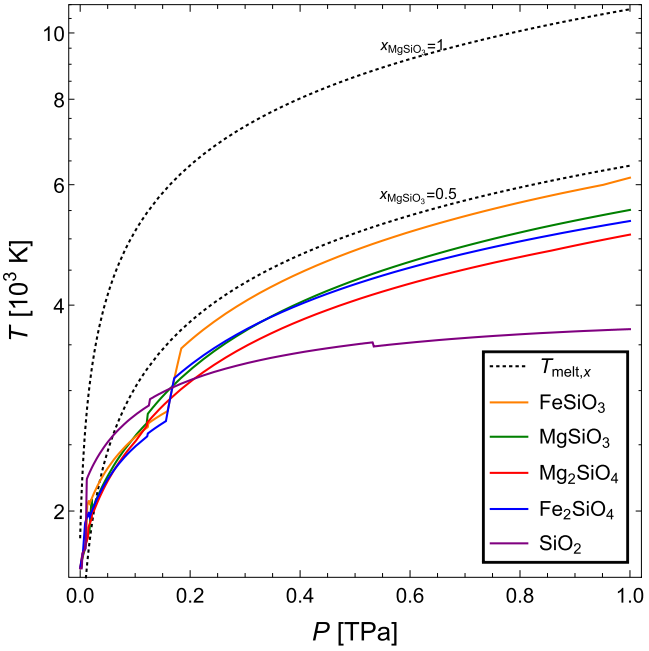


**Fig. 1.** Isentropes of the mantle mineralogy computed thermodynamically self-consistently with $T_S = 1650$ K. All relevant phases of $Mg_2SiO_4$, $Fe_2SiO_4$, $MgSiO_3$, $FeSiO_3$ and $SiO_2$ are taken into account. Dotted lines represent the melting temperature of $MgSiO_3$, $T_{melt} = 1831K(1 + P/4.6GPa)^{0.33}$ (Belonoshko et al., 2005) with the cryoscopic equation $T_{melt,x} = T_{melt}(1 - \ln x_{MgSiO_3})^{-1}$ (Atkins, 1994), where $x_{MgSiO_3}$ is the mole fraction of pure $MgSiO_3$. (For interpretation of the references to color in this figure legend, the reader is referred to the web version of this article.)

sume that there is no thermal boundary, corresponding to very efficient cooling of the core. In the second case, we assume that the temperature of the core at the CMB ($T_{CMB}$) is equal to the melting temperature of $MgSiO_3$ (e.g., Stixrude, 2014), $T_{CMB} = 1831K(1 + P/4.6GPa)^{0.33}$ (Belonoshko et al., 2005). Such an assumption combined with an isentropic mantle leads to an extreme temperature jump of ~2500–7000 K depending on the mantle temperature at the CMB. These values are higher than the temperature jumps of 800–2000 K used by Sotin et al. (2007), Valencia et al. (2007) and Wagner et al. (2011) and serve as upper bounds in our study.

We solve for $P$ and $g$ using Eqs. (1) and (2) and an equation of state corresponding to the composition of the core or the mantle. We apply six boundary conditions: $g(0) = 0$, $P(R) = 0$ and $T_S = 1650$ K, two conditions expressing the continuity of $P$ and $g$ at the CMB; $T$ at the CMB is either continuous or equal to the melting temperature of the mantle. In calculations of model super-Earths, we fix $R$ and the core radius fraction $r_{CMB}$ to compute $M$. In calculations of a super-Earth with given $M$ and $R$, we compute $r_{CMB}$.

### 2.2. Mantle modeling

In the context of rocky exoplanets, the mantle is commonly assumed to be made up of MgO end-member silicate minerals and the composition is usually assumed to be $MgSiO_3$ or $Mg_2SiO_4$ (e.g., Seager et al., 2007; Wagner et al., 2011). However, a mantle with only MgO and $SiO_2$ is unlikely to appear in nature. Mantle minerals are expected to also incorporate oxides CaO, FeO and $Al_2O_3$ in addition to MgO and $SiO_2$, the CFMAS system, which makes up for about 99 wt% of the bulk silicate Earth (Javoy et al., 2010). Neglecting FeO, CaO and $Al_2O_3$ bearing minerals that could be present in significant amounts and which mostly have higher densities than the end-member minerals in the MgO-$SiO_2$ system, would create a bias in the inference of the exoplanet's interior structure from mass and radius. Valencia et al. (2006) therefore evaluated the effect of FeO on the planetary structure by adding up to 10 wt% of FeO to $Mg_2SiO_4$ in the upper mantle and to $MgSiO_3$ in the lower mantle.

The exact oxide content of the mantle depends on several factors including stellar composition, origin of the building blocks in the protoplanetary disk, planetary migration, the degree of differentiation in the planet and redox conditions in the mantle (e.g., Bond et al., 2010; Carter-Bond et al., 2012b; Dorn et al., 2015; Schaefer et al., 2017; Santos et al., 2017). Although data are currently missing to accurately assess realistic ranges in compositions of exoplanetary mantles, significant deviations with respect to the mantle compositions of the terrestrial planets of the solar system are to be expected. Rocky exoplanets can for example be extremely depleted in Mg compared to the Earth, as has been shown by N-body simulations for the HD17051 and HD19994 planetary systems by Carter-Bond et al. (2012a). Here we consider five different end-member compositions: $MgSiO_3$, $FeSiO_3$, $Mg_2SiO_4$, $Fe_2SiO_4$ and $SiO_2$, thereby extending the range of mantle compositions with respect to previous studies. The FeO end-members of olivine and bridgmanite, although much less likely than MgO end-members, represent an upper bound on the mantle density as they are the highest density minerals in the respective solid solutions (Stixrude and Lithgow-Bertelloni, 2011).

Phase relations and physical properties of mantle minerals are evaluated self-consistently using a new implementation (Chust et al., 2017) of the thermodynamic model of Stixrude and Lithgow-Bertelloni (2011) based on a Birch–Murnaghan Mie–Grüneisen equation of state formulation. At least for density, the central property we are interested in, the model shows robust behavior beyond the $P$-$T$ conditions of the lowermost mantle (Connolly and Khan, 2016). From the database of Stixrude and Lithgow-Bertelloni (2011), we use MgO, the $SiO_2$ phases as well as the MgO- and FeO-bearing end-members of all silicate solid solutions to compute assemblages for the compositions given above. As the database of Stixrude and Lithgow-Bertelloni (2011) is only assessed for conditions (and minerals) of the Earth's mantle and ignores phase transitions at higher pressures, such as the dissociation of post-perovskite (ppv) (e.g., Umemoto and Wentzcovitch, 2011; Wu et al., 2014) or the B1-B2 transition in MgO (e.g., Cebulla and Redmer, 2014), we investigate an alternative scenario for mantle structure (Section 5.3), taking high-pressure phases and transitions from Umemoto and Wentzcovitch (2011) into account.

The isentropes associated with the five model compositions and the potential temperature of 1650 K are shown in Fig. 1. Isentropes show $T$-discontinuities at phase transitions with significant Clausius–Clapeyron slopes through volume changes and latent heat effects. Mostly, temperatures increase as different compositions undergo phase transitions with positive Clapeyron slopes. The perovskite-ppv transition in the $MgSiO_3$ and $Mg_2SiO_4$ compositions in the vicinity of 100 GPa are such an example. The melting temperature of $MgSiO_3$ is higher than the temperatures along the isentropes of $MgSiO_3$ and $Mg_2SiO_4$, implying a solid mantle for super-Earths. The larger $T$-jumps for the FeO-bearing compositions at a pressure between 150–200 GPa stem from the formation of the $FeSiO_3$ ppv phase from a combination of $SiO_2$ seifertite and FeO wüstite, as the $FeSiO_3$ perovskite phase is predicted stable only at temperatures below 1500 K. For an $SiO_2$-only mantle, the stishovite-seifertite transition between 100–150 GPa leads to a temperature increase, but stishovite is then predicted to form again near 500 GPa with a negative Clapeyron slope and a slight temperature decrease. The re-appearance of stishovite is a numerical artifact of the database calibration, and a proper description of an $SiO_2$-based mantle would require an explicit consideration of the predicted high-pressure phases (Tsuchiya and Tsuchiya, 2011; Umemoto and Wentzcovitch, 2011). However, based on our discus-

sion in Section 5.3, such a consideration will not strongly affect the overall structure of super-Earths.

### 2.3. Core modeling

Iron is ubiquitously assumed to be the major element in the core of super-Earths (e.g., Seager et al., 2007; Wagner et al., 2011). To compute the density of Fe at relevant conditions, previous studies have extrapolated different formulations of the equation of state of Fe which are strictly speaking only valid within the pressure range of their assessment (see Table F.7). For instance, the Vinet formulations of Valencia et al. (2007) and Seager et al. (2007) and the third-order Birch-Murnaghan (BM3) formulation of Dorn et al. (2015) are fitted to data of Fe up to pressures of 200–300 GPa but extrapolated to 5–20 TPa. Neither the Vinet nor BM3 equations have extrapolations that are thermodynamically consistent to infinite pressure (e.g., Holzapfel, 1996; Stacey, 2005). Seager et al. (2007) switch to a Thomas-Fermi-Dirac equation of state at 20.9 TPa that is valid at in the infinite pressure limit. Wagner et al. (2011) have used the modified Rydberg equation (Stacey, 2005) and fitted the data from Dewaele et al. (2006), obtained between 17 and 197 GPa. Extrapolation to several tens of TPa will result in significantly different density predictions, depending on the equation used, even when those equations approach a thermodynamically consistent limit at infinite pressure. For this reason, we calculated an equation of state of iron for super-Earths (SEOS) up to 137 TPa with ab initio methods. With this equation of state the core of Earth-mass and ultra-massive super-Earths can be modeled without using a biasing extrapolation scheme. Details are discussed in Section 3.1.

For the Earth's core, Fe accounts for about 85 wt% and the remainder consists of Ni and light elements. For the light elements in the Earth's core, there is no consensus on their amount and identity. A recent synthesis of different studies about the composition by Hirose et al. (2013) suggest: Si = 6 wt%, O = 3 wt% and S = 1–2 wt%. Also, the possibility of C as a light element in the Earth's core cannot be ruled out (Fei and Brosh, 2014). In order to evaluate the effect of potentially important light elements in the core on mass-radius relations, we consider two approaches, reflecting the combined effects of Ni and light elements. First, we assume a decrease in density of the core with respect to pure iron by 10%, similar to the Earth's core; we also consider a decrease in density of 20%, i.e., we assume the core density to be either $0.9\rho$ Fe or $0.8\rho$ Fe. Second, in order to be able to assess the effect of the presence of specific light elements, we assume that the core is made of either of the following Fe-alloys: FeS, FeSi, $Fe_{0.95}O$, $Fe_3C$ (see Table D.5). For details about the equations of state, see Appendix D.

The melting curve of iron is steeper than a core isentrope at super-Earth pressures, suggesting that the core of massive super-Earths is solid if the temperature at the core-mantle boundary is below the melting temperature (Morard et al., 2011). The effect of light elements on the melting temperature of Fe at super-Earth core conditions is not known, but a maximal depression of 1500 K at 1.5 TPa has been proposed (Morard et al., 2011). The melting temperature of such an alloy is then above 13,000 K at 1.5 TPa and thus significantly above the predicted temperature at that pressure in super-Earth cores (Valencia et al., 2006; Wagner et al., 2012), indicating a solid core. Several factors including a sluggish or non-convecting lower mantle, warm initial conditions and a high temperature jump at the CMB (Stixrude, 2014) would allow for significantly higher core temperatures. Nevertheless, since the density deficit between the solid and the liquid state decreases with pressure (Alfè et al., 2002) and is about 1–2% at the inner core boundary conditions of the Earth (Alfè et al., 2002; Laio et al., 2000; Ichikawa et al., 2014), the use of an equation of state describing the density of solid iron has likely a negligible effect on mass-radius relations.

### 2.4. Mass-radius relations based on core size

Since mass and radius are currently the only observable parameters for most of the rocky exoplanets, mass-radius (*M-R*) relations are used to obtain a first-order estimate of their composition. Theoretical *M-R* relations of rocky planets have been computed for isothermal planetary interiors (e.g., Zapolsky and Salpeter, 1969; Seager et al., 2007) and temperature increasing with depth (e.g., Valencia et al., 2006; Fortney et al., 2007; Sotin et al., 2007; Wagner et al., 2011). Simple power-law relations are generally used for super-Earths:

$$R = aM^{\beta}, \tag{4}$$

where $R$ and $M$ are in Earth units, $\beta$ is the scaling exponent and $a$ is the proportionality constant. $\beta$ determines how the radius increases with mass: the larger $\beta$, the bigger are planets for the same mass. For small bodies whose internal density is not affected by pressure, $\beta = 1/3$. For larger planetary bodies, adiabatic self-compression leads to a slower increase of radius with mass and therefore smaller $\beta$.

Since the core size has a direct impact on planetary mass and bulk density, we calculate *M-R* relations for three classes of rocky super-Earths: Mercury-like, Earth-like and Moon-like by fixing core radius fractions to 0.8, 0.5 and 0.2, respectively. These values are similar to those of Mercury (0.82), the Earth (0.54) and the Moon (0.21) (e.g., Dziewonski and Anderson, 1981; Garcia et al., 2011; Hauck et al., 2013; Rivoldini and Van Hoolst, 2013). Our definition of rocky super-Earth classes contrasts with most previous studies (e.g., Valencia et al., 2006; Wagner et al., 2011) in which the core mass fraction and essentially the bulk elemental composition of an exoplanet class is constant but the relative core radius changes along a *M-R* relationship. With our definition, the bulk composition of super-Earths of a given class slightly varies with mass (e.g., elemental abundance of Mg changes by <2 wt%) since the relative core radius is constant. This difference results in small differences of the order of 1–4% in the $\beta$ values of the *M-R* relations. In order to be able to make consistent comparisons with the literature, we recompute $\beta$ values for previous studies based on the same interior structure assumptions as in our work (see Table 2). We also compute *M-R* relations for bare-core super-Earths since observations suggest their existence (Mocquet et al., 2014). Such a calculation provides an upper bound on the masses of super-Earths as a function of radius.

## 3. A new ab initio equation of state of hcp-Fe

### 3.1. Formulation of SEOS

Laser-heated diamond-anvil cell experiments (Sakai et al., 2011) show that the crystal structure of pure Fe at the conditions of the Earth's core is hexagonal close-packed (hcp). However, high core temperatures (Belonoshko et al., 2017), the presence of nickel (Dubrovinksy, 2007) and light elements in the core (Vočadlo et al., 2003) could stabilize the body-centered cubic (bcc) phase over hcp at the Earth's inner-core conditions. The exact crystal phase of the Earth's inner core remains a matter of extensive debate, but hcp-Fe is the most plausible candidate (e.g., Hirose et al., 2013).

Ab initio crystal structure predictions at zero temperature show that hcp-Fe is more stable than bcc and fcc up to 8 TPa and between 24–35 TPa (e.g., Pickard and Needs, 2009; Cottenier et al., 2011), and this remains true up to at least 10,000 K (Stixrude, 2012). Between 8–24 TPa, the face-centered cubic (fcc) phase is stable and above 35 TPa the bcc phase takes over. Since

the expected core pressures in Earth-like super-Earths are likely below 10 TPa (Wagner et al., 2011), their cores would be dominated by hcp-Fe if they are pure Fe and at zero temperature. However, as already mentioned, high temperature and alloying elements will likely change the stability fields of different phases. The exact phase at TPa pressures is probably not very important for mass-radius relations of super-Earths since the density difference between the crystal phases of iron is expected to be small, especially for the closed-packed phases. According to the calculations in Cottenier et al. (2011), at 350 GPa fcc is 0.05% less dense than hcp, while bcc is 1.2% less dense. At higher pressures, density differences remain small: At 8 TPa, fcc and bcc are denser than hcp by less than 0.1%. For this reason, we approximate iron in the core of super-Earths as the hcp phase.

Here we perform Density Functional Theory (DFT)-based calculations for hcp-Fe in the volume range of 0.50-6.79 $cm^3$/mol, to cover the whole compression range relevant for the cores of super-Earths. For high precision, we use the all-electron augmented plane wave method with local orbitals (APW+lo) (Schwarz et al., 2010; Sjöstedt et al., 2000; Madsen et al., 2001; Cottenier, 2002) with the PBE approximation to the exchange and correlation fuctional (Perdew et al., 1996). Within the APW+lo approach, we treat the 3*s*, 3*p*, 3*d*, 4*s*, 4*p* states as valence electrons. The muffin tin radius for the Fe-atoms was set to 1.6 au, and the size of the APW+lo basis specified by $K_{max} = 8.5/1.6$ au $= 5.31$ au$^{-1}$. Brillouin zone integration used a mesh of $42 \times 42 \times 22$ *k*-points. Calculations were performed both for non spin-polarized and spin-polarized charge densities, using the type II spin arrangement of Steinle-Neumann et al. (2004). At each volume, the *c*/*a* ratio was optimized and we found an increase with compression from 1.5858–1.6165 in the range from 0–2.5 TPa (1.6033 at 350 GPa).

From the energy-volume relation of 181 values (Appendix G) pressure is computed as the first derivative numerically. We employ an averaged 2-point backward and forward scheme that takes into account the uneven volume sampling. We chose this strategy, as the energy-volume range sampled by our calculations is too large to be adequately fit with a single closed expression (Fig. B.10). Without a closed expression for the equation of state, we obtain volumes at given pressure by an interpolation scheme: this is done with a method that uses a sliding-window to locally fit a finite strain expression (see Appendix C for a detailed description).

In previous studies, several methods within the framework of DFT have been applied to calculate the equation of state of hcp-Fe, almost always with the Perdew–Burke–Ernzerhof (PBE) exchange-correlation functional or closely related ones and with a variety of numerical solvers. Our results at zero pressure (Table E.6) are in good agreement with published values, and the small differences are what can be expected when comparing different DFT codes (Lejaeghere et al., 2016a). Our density results are in excellent agreement with those of Pickard and Needs (2009) over a broad pressure range (cf. Fig. 1, Cottenier et al., 2011) and differ by less than 0.2% with the results of Stixrude (2012) at 6 and 38.3 TPa. The accuracy of DFT (PBE) predictions for a ground state equation of state (equilibrium volume or density, bulk modulus) have been assessed by Lejaeghere et al. (2013, 2016b). In particular when the bulk modulus is large, as in the present work, the uncertainty on the predicted density becomes negligibly small (Lejaeghere et al., 2016b).

Measurements of compression data at room temperature provide a reliable equation of state for iron up to almost 300 GPa (e.g., Fei et al., 2016): the third-order Birch–Murnaghan equation (BM3) used to summarize new and previous experimental data have pressure residuals that are not much larger than 2%. A fit of the same data to a Vinet equation (e.g., Poirier, 2000) results in similar residuals and the predicted bulk moduli from both equations are equivalent (see Fig. A.9). The induced uncertainty on the parameters of the BM3 equation by the data uncertainties results in an error on density that is smaller than 0.5% and that on the bulk modulus is smaller than 1% at 300 GPa. In order to use the laboratory measurements together with the DFT results, the former have been extrapolated to 0 K (Fei et al., 2016) and zero-point vibration effects have been removed (Lejaeghere et al., 2014). The equations based on prior experimental data (e.g., Williams and Knittle, 1997; Anderson et al., 2001; Dewaele et al., 2006) show deviations from the equation of state of Fei et al. (2016) and SEOS (based on the same low pressure data) that are larger than 0.5% (Fig. 2) because they have either been deduced from smaller data sets or/and the uncertainties on those data were larger.

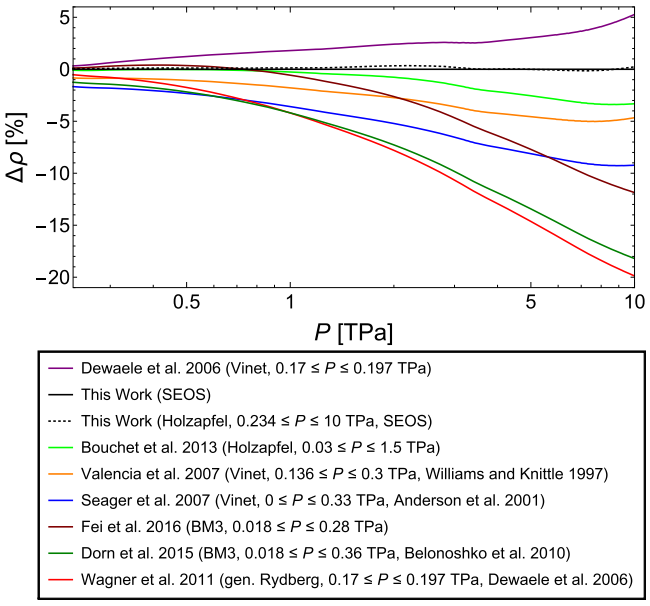


**Fig. 2.** Comparison of the relative density difference in per cent for equations of state of iron listed in Table F.7 and for the Holzapfel fit to SEOS up to 10 TPa relative to SEOS at 0 K in the pressure range of 0.234–10 TPa. These equations of state are indicated by references, the form of the equation used, the pressure range of the fit and, if applicable, the source of the data. (For interpretation of the references to color in this figure legend, the reader is referred to the web version of this article.)

Our DFT results for hcp exhibit the well known pressure underestimation of about 8% at small compressions (Steinle-Neumann et al., 2004; Fei et al., 2016) (Fig. E.11), an effect that cannot be explained by thermal pressure alone (less than 1%) and for which dynamical many-body effects beyond DFT need to be invoked (Pourovskii et al., 2014). This discrepancy is larger than what is usually obtained using DFT at the PBE level, including for bcc-Fe where the agreement with experiments is excellent (see Lejaeghere et al., 2014). After correcting laboratory data of hcp-Fe for thermal effects, densities become comparable to DFT results near 200 GPa. At pressures higher than 300 GPa, and depending on the formulation used to summarize the experimental data, extrapolated pressures grow weaker or stronger than our DFT results with compression (see Fig. 2 and discussion below). Therefore, we use the experimental equation of state of hcp iron for pressures up to 234 GPa, the pressure where laboratory data and our DFT results intersect, and our DFT results for pressures above. A discontinuity in $K_T$ of $\sim$10% between the experimental equation of state and our DFT results has a negligible effect on mass-radius relations and a small effect on the thermal state of the core.

In addition to the numerical determination of SEOS that we have introduced above, we include, for convenience, a closed equation of state that is valid for pressures above 234 GPa. When the Holzapfel equation (Holzapfel, 1996) is fitted to our ab initio results in the pressure range 0.234–10 TPa, the volume residuals are

below 1.1%, whereas fits with BM3 or Vinet equations have residuals that are 4 to 8 times larger. The Holzapfel equation is written as

$$P = P_0 + 3K_{T,0}x^{-\frac{5}{3}}\left(1-x^{\frac{1}{3}}\right)\left[1+c_2x^{\frac{1}{3}}\left(1-x^{\frac{1}{3}}\right)\right]\exp\left[c_0\left(1-x^{\frac{1}{3}}\right)\right], \quad (5)$$

where $x = V/V_0$, $V_0 = 4.28575$ cm$^3$/mol, $P_0 = 234.4$ GPa, $K_{T,0} = 1145.7 \pm 3.6$ GPa, $c_0 = 3.19 \pm 0.08$ and $c_2 = -2.40 \pm 0.05$.

### 3.2. Thermal pressure

Total pressure can be divided into a cold (isothermal) part (discussed above), and two temperature-dependent (thermal) parts: $P(V,T) = P(V, 0\ \text{K}) + P_{\text{harm}}(V,T) + P_{\text{ae}}(V,T)$, where $P_{\text{harm}}$ is the quasiharmonic thermal pressure and $P_{\text{ae}}$ is the anharmonic-electronic thermal pressure. For the quasiharmonic thermal pressure, phonon calculations can be performed (e.g., Vočadlo et al., 2008; Stixrude, 2012) or approximated by the Debye (e.g., Dewaele et al., 2006; Fei et al., 2016) or Einstein models (e.g., Bouchet et al., 2013). At high temperatures in the core of super-Earths, well above the Debye temperature, the Einstein and Debye models practically coincide (Poirier, 2000). Following Bouchet et al. (2013), we use the simpler Einstein model to compute $P_{\text{harm}}$ and the Einstein temperature $\Theta$:

$$P_{\text{harm}}(V,T) = \frac{3R\gamma}{V}\left[\frac{\Theta}{2} + \frac{\Theta}{\exp(\Theta/T)-1}\right], \quad (6)$$

$$\Theta = \Theta_0 x^{-\gamma_\infty}\exp\left[\frac{\gamma_0-\gamma_\infty}{b}(1-x^b)\right], \quad (7)$$

with the Grüneisen parameter $\gamma = \gamma_\infty + (\gamma_0 - \gamma_\infty)x^b$, where $R$ is the universal gas constant, $b$ is a constant and $x = V/V_0$. The approach of Bouchet et al. (2013) reproduces the experimental $P-V-T$ equation of Dewaele et al. (2006) well that is fit to static and shock wave experiments as well as ab initio simulations. The anharmonic-electronic thermal pressure is given as

$$P_{\text{ae}}(V,T) = \frac{3R}{2V}ma_0x^mT^2, \quad (8)$$

where $m$ and $a_0$ are constants.

For both the harmonic and anharmonic-electronic thermal pressure we use the parameter values estimated by Bouchet et al. (2013) (see Table F.7). Since our reference volume $V_0$ is not the same as that of Bouchet et al. (2013), we replace $x$ in the equations for the quasiharmonic and anharmonic-electronic thermal pressures by $x\,(V_0/V_{0,\text{ Bouchet}})$. With this modification, the thermal pressure is equal to that of Bouchet et al. (2013) for a given volume $V$.

The isothermal bulk modulus $K_T$, the isobaric thermal expansivity $\alpha$ and the adiabatic bulk modulus $K_S$ are given by

$$K_T = -V\left(\frac{\partial P(V,T)}{\partial V}\right)_T, \quad (9)$$

$$\alpha = \frac{1}{V}\left(\frac{\partial V}{\partial T}\right)_P, \quad (10)$$

$$K_S = K_T(1+\alpha\gamma T). \quad (11)$$

### 3.3. Comparison of extrapolations of the equations of state of iron

We compare previously published equations of state of Fe (see Table F.7) with our equation of state for super-Earths (SEOS) in the pressure range 0.234–10 TPa at 0 K. The various equations determined at a finite temperature were corrected to 0 K according to the method described in the respective articles and the zero-point vibration effects have been removed.

The BM3, Vinet, modified Rydberg and Holzapfel equations describe compression data with similar precision below 0.3 TPa if no prior assumption on equation parameters are made (see Appendix A), but extrapolation yields significantly different predictions at high pressures (see Fig. 2). Among those equations, the modified Rydberg and Holzapfel equations show a consistent thermodynamic behavior at infinite pressure and should therefore be used if large pressure extrapolations are required. The relevance of this behavior is illustrated by the equation of state from Bouchet et al. (2013) at 10 TPa (Fig. 2). Its density deviates by not much more than 3% from SEOS. In principle, a similar precision could be obtained with the modified Rydberg equation (see Appendix B), but the large deviations exhibited by the equation of state from Wagner et al. (2011) at 10 TPa (Fig. 2) is the result of their choice of a specific value for the derivative of the bulk modulus at infinite pressure prior to fitting the laboratory data of Dewaele et al. (2006).

Extrapolations with the Vinet formulation depart by more than 5% from SEOS at 10 TPa (Fig. 2) and deviations increase further with pressure. The large variations between the equations of state by Dewaele et al. (2006); Seager et al. (2007) and Valencia et al. (2007) at high pressure are the result of the different data sets used (see Table F.7). Among the equations considered, the BM3 equation is the least well suited for large pressure extrapolation (see Appendix A) and should be avoided. Note, however, that extrapolation of the equation of state up of Fei et al. (2016) to 1 TPa results in a density less than 0.5% different from that of SEOS. This is a consequence of the extensive and precise data set used to fit the BM3 equation.

## 4. Effect of the iron equation of state on M-R relations

To assess the effect of the choice of an equation of state of iron on the *M-R* relations of rocky super-Earths, we have calculated the masses of Moon-like, Earth-like, Mercury-like and bare-core super-Earths with radius between 1–2 $R_\oplus$ by solving the interior structure equations (Table 1 and Fig. 3). For the purpose of this argument, the core and mantle compositions are approximated to be pure Fe and $MgSiO_3$. We use $T_S = 1650$ K and ignore a temperature jump due to the thermal boundary layer at the CMB. Temperature profiles within the core and mantle are considered to be isentropic. We perform these calculations using SEOS and other equations of state of iron as discussed above.

Central density, temperature and pressure increase with the core radius fraction and with planetary radius (Table 1). The core mass fractions of Moon-like, Earth-like and Mercury-like super-Earths are in the range 2–3%, 29–36% and 76–83%, respectively. Thermal contributions to total pressure decrease with increasing central pressure. Similarly, the anharmonic-electronic contribution to thermal pressure decreases, but remains at a 10% level. It decreases the density by 1.6% at zero pressure and by 0.1% at 10 TPa. The resulting effects on *M-R* relations are not discernible.

Differences in computed planetary masses for different equations of state of iron are negligible for the Moon-like scenarios and $R = 1.25\ R_\oplus$, but they generally increase with increasing central pressure (Table 1). For the same planetary radius and larger core size, the mass predicted with some equations (Dorn et al., 2015; Wagner et al., 2011) reach differences by as much as −12% for a bare core planet. When increasing the planetary radius from 1.25–1.75 $R_\oplus$, differences are already noticeable for the smallest core radius fraction, and generally increase by a factor of 2–3 with core size; only for the equation of state by Dewaele et al. (2006) differences increase more strongly. All planetary models based on the equation of state of Dewaele et al. (2006) and some of the

**Table 1**
Interior structure parameters and differences in planetary mass between SEOS and other equations of state of iron for different core sizes and planetary radii. Differences below 0.05% are not reported. Models assume an isentropic pure Fe core, an isentropic $MgSiO_3$ mantle, $T_S = 1650$ K and a zero CMB $T$-jump.

| Ref. | Form. | Parameter | Bare-core | Mercury-like | Earth-like | Moon-like | Bare-core | Mercury-like | Earth-like | Moon-like |
|---|---|---|---|---|---|---|---|---|---|---|
| | | $r_{CMB}$ | 1 | 0.8 | 0.5 | 0.2 | 1 | 0.8 | 0.5 | 0.2 |
| | | $R$ ($R_\oplus$) | 1.25 | | | | 1.75 | | | |
| SEOS | – | $P_c$ (TPa) | 4.6 | 2.5 | 0.9 | 0.3 | 37.8 | 16.8 | 4.0 | 1.2 |
| | | $P_{th,\,c}/P_c$ | 3% | 4% | 7% | 11% | 1% | 2% | 4% | 6% |
| | | $P_{ae,\,c}/P_{th,\,c}$ | 14% | 17% | 20% | 22% | 8% | 12% | 16% | 19% |
| | | $T_c$ ($10^3$ K) | 8.6 | 7.2 | 5.1 | 3.7 | 18.2 | 15.4 | 9.1 | 5.8 |
| | | $\rho_c$ (Mg/m$^3$) | 30.4 | 24.4 | 17.7 | 13.6 | 66.1 | 48.9 | 28.8 | 19.1 |
| | | $M_{core}/M$ | 100% | 79.3% | 31.0% | 2.4% | 100% | 83.0% | 33.7% | 2.4% |
| | | $M$ ($M_\oplus$) | 6.5 | 4.0 | 2.2 | 1.7 | 33.6 | 18.7 | 8.4 | 5.9 |
| Dew | Vin | $\Delta M$ | + 1% | + 1% | + 0.5% | – | + 13% | + 10% | + 1.6% | + 0.2% |
| Bou | Hol | $\Delta M$ | −1% | −1% | – | – | −6% | −5% | −0.8% | – |
| Val | Vin | $\Delta M$ | −2% | −1% | – | – | −7% | −7% | −1.7% | – |
| Sea | Vin | $\Delta M$ | −5% | −3% | – | – | −18% | −14% | −3.1% | – |
| Fei | BM3 | $\Delta M$ | −3% | −1% | + 0.5% | – | −22% | −14% | −1.9% | – |
| Dor | BM3 | $\Delta M$ | −13% | −7% | −1.4% | – | −34% | −23% | −5.7% | −0.2% |
| Wag | Ryd | $\Delta M$ | −12% | −6% | −1.4% | – | −35% | −24% | −6.0% | −0.2% |

Abbreviations: SEOS: Super-Earths equation of state, This Work, $P_{th}$ from Bouchet et al. (2013); Dew: Dewaele et al. (2006); Bou: Bouchet et al. (2013); Val: Valencia et al. (2007), data from Williams and Knittle (1997); Sea: Seager et al. (2007), data from Anderson et al. (2001); Fei: Fei et al. (2016); Dor: Dorn et al. (2015), data from Belonoshko et al. (2010); Wagner et al. (2011), data from Dewaele et al. (2006); Vin: Vinet; BM3: third-order Birch-Murnaghan; Hol: Holzapfel; Ryd: modified Rydberg.

**Table 2**
Mass-radius relation scaling exponent $\beta$, calculated using different equations of state of Fe. Models assume an isentropic pure Fe core, an isentropic $MgSiO_3$ mantle, $T_S = 1650$ K and a zero CMB $T$-jump. Our calculations for $\beta$ values, using the equations of state from the studies listed below, are performed by fixing the core radius fraction. In the mass-radius relation, $R/R_\oplus = a(M/M_\oplus)^\beta$, $a$ is 0.82, 0.89, 1.02 and 1.08 for bare-core, Mercury-like, Earth-like and Moon-like super-Earths, respectively.

| Equation of state | Bare-core | Mercury-like | Earth-like | Moon-like |
|---|---|---|---|---|
| $r_{CMB}$ | 1 | 0.8 | 0.5 | 0.2 |
| SEOS, $P_{th}$ from Bouchet et al. (2013) | 0.218 | 0.232 | 0.252 | 0.270 |
| Dewaele et al. (2006), Vinet | 0.207 | 0.224 | 0.248 | 0.269 |
| Bouchet et al. (2013), Holzapfel | 0.224 | 0.238 | 0.253 | 0.270 |
| Valencia et al. (2007), Vinet[a] | 0.225 | 0.240 | 0.255 | 0.270 |
| Seager et al. (2007), Vinet[b] | 0.237 | 0.248 | 0.258 | 0.270 |
| Fei et al. (2016), BM3 | 0.242 | 0.248 | 0.257 | 0.270 |
| Dorn et al. (2015), BM3[c] | 0.251 | 0.255 | 0.260 | 0.270 |
| Wagner et al. (2011), mod. Rydberg[d] | 0.255 | 0.259 | 0.262 | 0.270 |

Abbreviations: $P_{th}$: Thermal Pressure. BM3: ithird-order Birch-Murnaghan equaton. Data source: [a] Williams and Knittle (1997), [b] Anderson et al. (2001), [c] Belonoshko et al. (2010), [d] Dewaele et al. (2006).

1.25 $R_\oplus$ Earth- and Mercury-type models (based on the equations from Bouchet et al., 2013; Fei et al., 2016; Seager et al., 2007) yield a larger planetary mass due to larger densities over the relevant $P$-$T$ range. This difference either stems from the isothermal equation of state (Fig. 2) or a smaller thermal pressure contribution than in SEOS. A comparison of differences in $M$-$R$ relation over a wider size range (Fig. 3) confirms this trend.

Looking at the effect of different equation of state formulations for iron on the mass of super-Earths with an Earth-like core ratio, Wagner et al. (2011) found a difference of 2% in radius for 10 $M_\oplus$, using modified Rydberg and Keane equations, based on the same experimental data of iron from Dewaele et al. (2006). Interestingly, we find that the use of the Vinet equation of Dewaele et al. (2006), still based on the same data, leads to a smaller radius by 3% compared to the modified Rydberg equation from Wagner et al. (2011) for a 10 $M_\oplus$ Earth-like model. As explained above, this discrepancy stems from their choice of a specific value for the derivative of the bulk modulus at infinite pressure.

The differences in radii calculated using the two equations of state of iron with maximum density difference are 1% and 2% ($M = 1\ M_\oplus$), 2% and 4% ($M = 5\ M_\oplus$), and 3% and 6% ($M = 10\ M_\oplus$) for Earth-like and Mercury-like super-Earths, respectively. Such differences result in significant variations for the exponent $\beta$ in the mass-radius scaling law (Eq. (4)), and values for $\beta$ can vary by as much as 10% (Table 2). These differences are a consequence of extrapolations of the equations meant to be used up to the pressures of ~0.3 TPa. Since the Holzapfel equation from Bouchet et al. (2013) needs to be extrapolated starting at 1.5 TPa, its $M$-$R$ curves diverge significantly from those based on SEOS for super-Earths with larger cores or larger planetary radii only (Fig. 3).

## 5. Effects of temperature and composition on M-R relations

### 5.1. Temperature

Since the temperature profile in super-Earths is not well constrained, it is important to assess the effect of uncertainties in temperature on the structure of super-Earths. Previous studies indicate a relatively minor effect (e.g., Sotin et al., 2007; Grasset et al., 2009). Here we re-evaluate this effect for some of the temperature assumptions described in Section 2.

For Moon-like models, a change in the temperature profile in the core from isentropic to isothermal reduces the central temperature by 200–600 K and has a negligible impact on mass. For Earth-like and Mercury-like models, the differences between the isentrope and isotherm in the center are 1000–4500 K and 2500–10000 K and masses by up to 1% and 2%, respectively.

An extreme CMB temperature jump of around 2500–7000 K (see Section 2) reduces the density of the core, it has a negligible impact on Moon-like models, but decreases the mass of Earth-like and Mercury-like super-Earths between 1–2% and 2–5%, respectively. This temperature jump effect decreases with planetary radius because thermal contribution to pressure de-

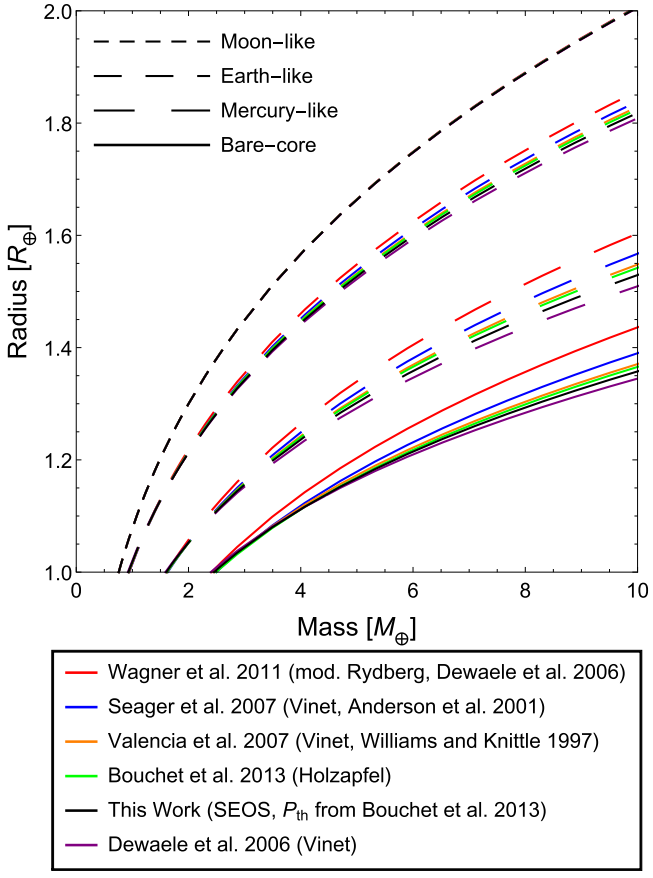


**Fig. 3.** Effects of selected equations of state of Fe from Table F.7 on the mass-radius relations of four classes of super-Earths with fixed core radius fractions. (For interpretation of the references to color in this figure legend, the reader is referred to the web version of this article.)

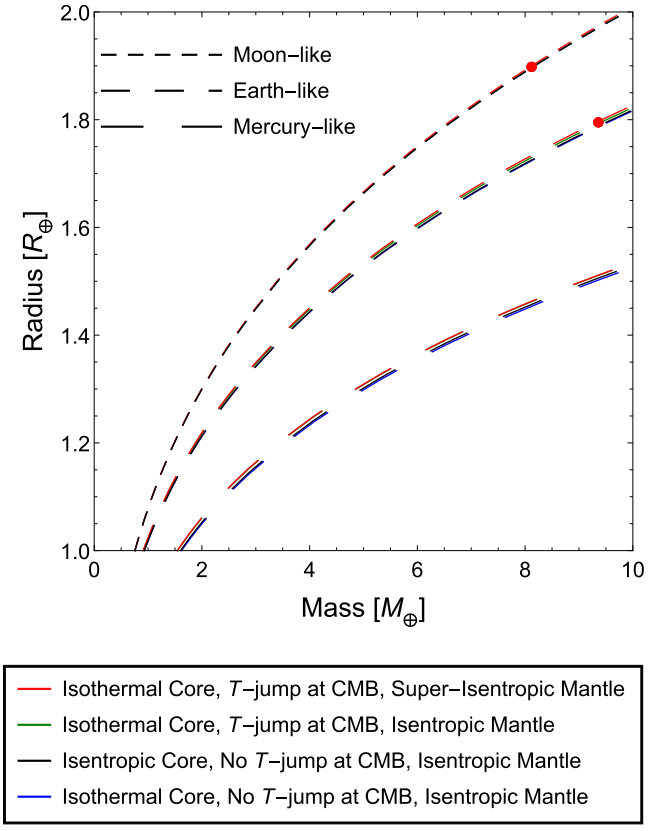


**Fig. 4.** Effects of temperature on mass-radius relations of super-Earths with fixed core radius fractions. Red dots on red lines represent the mass and radius where the CMB temperature is at the solvus. For Mercury-like super-Earths, the cut-off occurs for planets with $M > 10\ M_\oplus$. (For interpretation of the references to color in this figure legend, the reader is referred to the web version of this article.)

creases. Conversely, for a given planetary mass, the planetary radius increases by up to 1% and 1.5% for Earth-like and Mercury-like models (Fig. 4). These results are comparable to those of Grasset et al. (2009) who found a difference of up to 2% in radius when varying the planetary temperature profiles by 4000 K. To summarize, the effect of the core thermal profile and the CMB temperature jump on *M-R* relations increases with core size.

In the lower mantle, a super-adiabatic thermal gradient, starting at the transition to Mg-ppv, leads to a decrease in the mass of super-Earths by up to 3%. This effect is most prominent for moderate size cores (Earth-like) since smaller or larger cores lead to a smaller super-adiabatic profile in the mantle because the pressure either increases more slowly with depth or the mantle is thinner. In the super-adiabatic case, if the temperature in the lower mantle is higher than the solvus temperature of MgO, parts of the lower mantle might be soluble in the iron core (Wahl and Militzer, 2015). Our calculations for a pure Fe core show that the miscibility of rock and iron can occur when $R_{\text{Moon-like}} > 1.9\ R_\oplus$, $R_{\text{Earth-like}} > 1.8\ R_\oplus$ and $R_{\text{Mercury-like}} > 1.75\ R_\oplus$ (see Fig. 4). For such planets, the core size is defined by the solvus. If the core contains light elements, the pressure at the CMB for a given planet radius is lower than in a planet with a pure Fe core, therefore a dissolution of the lower mantle in the core occurs for planets with larger radii than for the pure Fe core case.

Overall, the effect of temperature on mass-radius relations is smaller than the effect of extrapolations of the equations of state of iron as seen in Figs. 3 and 4. Mass-radius relations due to changes in temperature profile differ only by $\Delta\beta < 0.003$ for all cases considered here. This confirms the results obtained by e.g., Sotin et al. (2007) and Grasset et al. (2009) and extends their validity range. Temperature, nevertheless, is important for many dynamic aspects of a planet, such as convection, volcanism as well as potential habitability.

### 5.2. Core composition

The composition of the core is one of the prime factors determining the mass of a super-Earth with a given radius (e.g., Unterborn et al., 2016). Valencia et al. (2007) showed that the presence of a relatively small amount of light elements in the core, smaller than the amount in the Earth's core, can change the radius of large super-Earths with given mass by a non-negligible amount. Here we quantify this effect for prescribed density deficits with respect to pure iron and compare results obtained for different core compositions. The effect on mass-radius relations is negligible for Moon-like super-Earths, but significant for planets with larger cores (Fig. 5).

Models with $Fe_3C$ cores are lighter than those with pure Fe cores resulting in smaller masses (Table 3). Super-Earths with $0.9\rho$ Fe cores are denser than FeS but lighter than $Fe_3C$. Models with FeS, FeSi or $Fe_{0.95}O$ cores have similar masses. Mass-radius curves with $0.8\rho$ Fe as core composition are almost overlapping with those of FeS, FeSi and $Fe_{0.95}O$ as core compositions, implying that the addition of 50 mol% (36 wt%) S, 50 mol% (33.5 wt%) Si or 51 mol% (23 wt%) O in the Fe-core is virtually equivalent to a 20% density deficit with respect to pure Fe. We do not show the overlapping *M-R* curves of the FeSi and $Fe_{0.95}O$ cases in Fig. 5. It is interesting to note that the mass-radius curve of Mercury-like super-Earth with a pure Fe core and a $MgSiO_3$ mantle overlaps with that

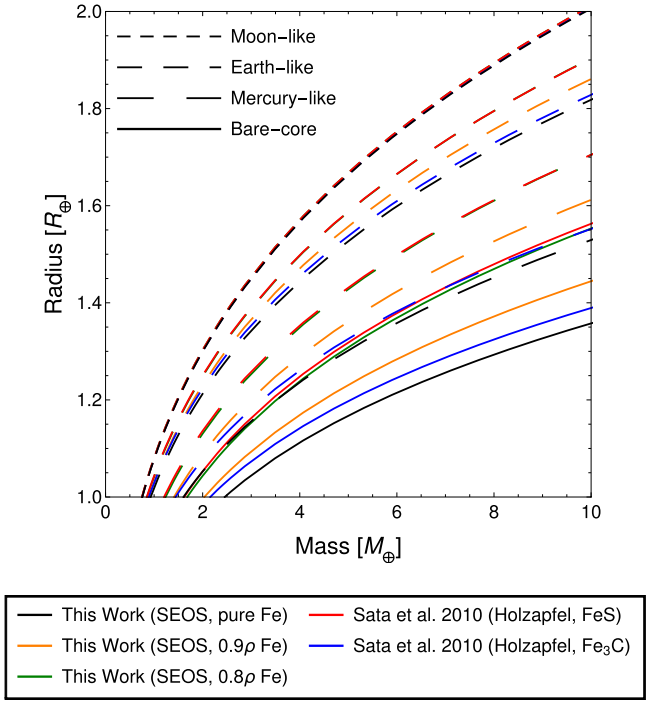


**Fig. 5.** Effect of different core compositions on mass-radius relations of super-Earths with fixed core radius fractions. The Moon-like, Earth-like and Mercury-like models for our 0.8$\rho$ Fe case and the FeS (Sata et al., 2010) case overlap with each other. Sata et al. (2010) measured the equation of state data of FeS and $Fe_3C$ up to ~200 GPa. (For interpretation of the references to color in this figure legend, the reader is referred to the web version of this article.)

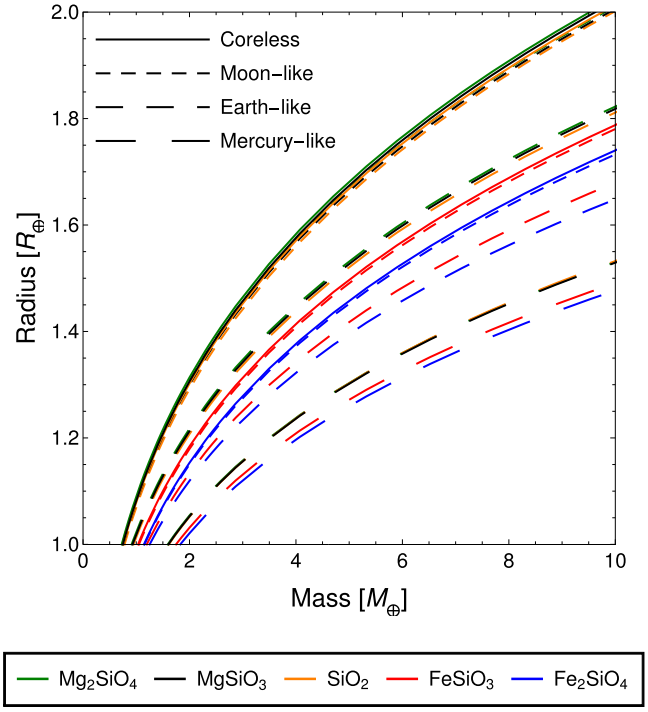


**Fig. 6.** Effect of different mantle compositions on mass-radius relations of super-Earths with fixed core radius fractions. Lines corresponding to $MgSiO_3$, $Mg_2SiO_4$ and $SiO_2$ almost overlap with each other, with $SiO_2$ being the most dense and $Mg_2SiO_4$ being the least dense among these three compositions. (For interpretation of the references to color in this figure legend, the reader is referred to the web version of this article.)

**Table 3**
Differences in planetary mass of super-Earths with $R$ = 1.25 $R_\oplus$ and $R$ = 1.75 $R_\oplus$ between different core compositions and core sizes. All differences in mass are calculated with respect to the model with a pure Fe core. Models assume an isentropic core, an isentropic $MgSiO_3$ mantle, $T_S$ = 1650 K and a zero CMB $T$-jump.

| Core comp. | Parameter $r_{CMB}$ | Bare-core 1 | Mercury-like 0.8 | Earth-like 0.5 | Moon-like 0.2 |
|---|---|---|---|---|---|
| $R$ = 1.25 $R_\oplus$ | | | | | |
| 0.9$\rho$ Fe | $\Delta M$ | −21% | −16% | −6% | −0.5% |
| 0.8$\rho$ Fe | $\Delta M$ | −38% | −28% | −11% | −0.6% |
| FeS | $\Delta M$ | −40% | −29% | −11% | −0.6% |
| FeSi | $\Delta M$ | −40% | −30% | −11% | −0.6% |
| $Fe_{0.95}O$ | $\Delta M$ | −43% | −31% | −12% | −1.2% |
| $Fe_3C$ | $\Delta M$ | −11% | −9% | −4% | −0.3% |
| $R$ = 1.75 $R_\oplus$ | | | | | |
| 0.9$\rho$ Fe | $\Delta M$ | −29% | −22% | −8% | −0.5% |
| 0.8$\rho$ Fe | $\Delta M$ | −50% | −39% | −15% | −1.0% |
| FeS | $\Delta M$ | −52% | −39% | −15% | −1.0% |
| FeSi | $\Delta M$ | −51% | −39% | −15% | −1.0% |
| $Fe_{0.95}O$ | $\Delta M$ | −49% | −37% | −14% | −1.0% |
| $Fe_3C$ | $\Delta M$ | −8% | −5% | −2% | −0.2% |

of FeS bare-core model, implying it is impossible to distinguish between the two with the knowledge of mass and radius only.

### 5.3. Mantle composition

Although mantle composition is mostly considered to be of lesser importance for the mass-radius relation of super-Earth exoplanets than core composition (e.g., Unterborn et al., 2016), only a limited range of mantle compositions has been considered previously. A reasonable range of mantle compositions based on stellar elemental ratios has been considered in Dorn et al. (2015), but these authors do not investigate their effect on mass-radius relations. As explained in Section 2, we here evaluate the effect of a wide range of mantle compositions and use the thermodynamic code of Chust et al. (2017) for the calculations of the various mineral phase transitions with increasing pressure. The effect of mantle composition on mass-radius relations increases with decreasing core size and increasing planetary radius (Fig. 6). Moon-like and coreless models have almost indistinguishable mass-radius relations because of the small cores of Moon-like models.

**Table 4**
Differences in planetary mass of super-Earths with $R$ = 1.25 $R_\oplus$ and $R$ = 1.75 $R_\oplus$ between different mantle compositions and core sizes. All differences in mass are calculated with respect to the model with a $MgSiO_3$ mantle. Models assume and isentropic pure Fe core, an isentropic mantle, $T_S$ = 1650 K and a zero CMB $T$-jump.

| Mantle comp. | Parameter $r_{CMB}$ | Mercury-like 0.8 | Earth-like 0.5 | Moon-like 0.2 | Coreless 0 |
|---|---|---|---|---|---|
| $R$ = 1.25 $R_\oplus$ | | | | | |
| $Mg_2SiO_4$ | $\Delta M$ | -0.8% | -1.4% | -2.4% | -2.4% |
| $SiO_2$ | $\Delta M$ | + 1.0% | + 2.3% | + 2.9% | + 3.0% |
| $FeSiO_3$ | $\Delta M$ | + 11% | + 32% | + 44% | + 58% |
| $Fe_2SiO_4$ | $\Delta M$ | + 15% | + 44% | + 44% | + 59% |
| $R$ = 1.75 $R_\oplus$ | | | | | |
| $Mg_2SiO_4$ | $\Delta M$ | -0.5% | -0.7% | -1.2% | -1.2% |
| $SiO_2$ | $\Delta M$ | + 3.0% | + 1.2% | + 1.5% | + 1.7% |
| $FeSiO_3$ | $\Delta M$ | + 15% | + 48% | + 63% | + 64% |
| $Fe_2SiO_4$ | $\Delta M$ | + 20% | + 63% | + 82% | + 83% |

Models with mantle compositions of $MgSiO_3$, $Mg_2SiO_4$ and $SiO_2$ differ by less than 2% (Table 4) because of the similarity in densities of MgO-$SiO_2$-based minerals. This finding extends that of Grasset et al. (2009) who showed that the effect of different Mg/Si ratios on planetary radius is <2%, but did not consider high-pressure mineral phase transitions of perovskite. Our calculations show that post-perovskite is the most abundant mineral in all Mg-rich super-Earths larger than the Earth. The dissociated assemblages of Mg-ppv (Umemoto and Wentzcovitch, 2011), $MgSi_2O_5$

+ MgO and $Fe_2P$-type $SiO_2$ + MgO, would be present in planets larger than $R \sim 1.7$ $R_\oplus$ and $R \sim 1.9$ $R_\oplus$, respectively. The inclusion of the dissociated phases of ppv has a negligible effect on the mass-radius relations of super-Earths.

The presence of FeO end-member minerals in the mantle increases the mass of the planet by a large amount, depending on the core size and the planetary radius (Table 4). For an Earth-like planet with $R$=1 $R_\oplus$, switching the mantle composition from $MgSiO_3$ to $FeSiO_3$ leads to a higher mass by 26%, comparable to the result of Unterborn et al. (2016). Even though FeO end-members do not represent realistic mantles, they give an upper-limit and illustrate the large effect of the Fe-content of the mantle on mass-radius relations.

### 5.4. M-R degeneracy and observed super-Earths

Uncertainties in mantle and core composition can introduce large errors in the determination of the core size of a rocky super-Earth without a gaseous envelope. In order to illustrate and quantify the combined effect of mantle and core compositions, we plot in Fig. 7 the mass-radius relations of bare-core, Mercury-like, Earth-like and Moon-like super-Earths with two extreme core compositions (pure Fe and 0.8$\rho$ Fe) and two extreme mantle compositions ($MgSiO_3$ and $FeSiO_3$). Since the effect of temperature is small, we restrict ourselves to one temperature profile. We assume an isentropic core with no temperature jump at the CMB. We also plot observed $M$-$R$ curves for planets with $R < 1.5\,R_\oplus$ from Weiss and Marcy (2014) and observed super-Earths[2], having uncertainties on radii and masses less than 10% and 50%, respectively.

In each of the four classes of super-Earths considered, the heaviest planets have a pure Fe core with a $FeSiO_3$ mantle and the lightest planets have a 0.8$\rho$ Fe core with a $MgSiO_3$ mantle. The colored bands in the $M$-$R$ plane in Fig. 7 represent the spread due to variations in mantle and core compositions. For Mercury-like super-Earths, the planets with a pure Fe core and a $MgSiO_3$ mantle are heavier than the planets with a 0.8$\rho$ Fe core and a $FeSiO_3$ mantle. However, the opposite is true for Earth-like and Moon-like planets which have smaller core size (Fig. 7(a)–(c)).

As an example of the degeneracy in estimating the core size due to uncertainties in mantle and core compositions we consider the case of CoRoT-7b. Its position in Fig. 7(b) on the Earth-like mass-radius curve with a pure Fe core and a $MgSiO_3$ mantle suggests that the core radius fraction of CoRoT-7b is about $\sim$0.5, for a pure Fe core and a $MgSiO_3$ mantle. A Mercury-like core size can be ruled out based on Fig. 7(c). On the other hand, given the position of CoRoT-7b in Fig. 7(a), it can also be Moon-like ($r_{CMB} \sim 0.2$) with a pure Fe core and a mantle in composition close to $FeSiO_3$. Uncertainties on the mass and radius of CoRoT-7b (15% and 4%, respectively) further contribute to the difficulty of constraining the core size. Additional information about composition, perhaps from the stellar composition as suggested by Dorn et al. (2015), is needed to lift the degeneracy.

For super-Earths with more extreme locations on the $M$-$R$ diagram, the degeneracy can be weaker. For example, HD 219134f, which is more massive than the Mercury-like or 0.8$\rho$ Fe bare-core super-Earths (see Fig. 7(c) and (d)), is likely the stripped-off core of a giant planet as suggested for some other planets by Mocquet et al. (2014). Super-Earths that lie above the mass-radius bands, even with the lightest pure $MgSiO_3$ composition, e.g., TRAPPIST-1f, have a lower density than a planet made purely of silicates (Fig. 7a) and likely contain significant amounts of lighter material such as ice or water in addition to rock. Another super-Earth in the same planetary system, TRAPPIST-1c, is situated in the denser part of the band of Earth-like models, and likely has a core radius fraction between that of the Earth and Mercury, assuming it has an Earth-like composition in the core and the mantle. The uncertainties on its mass, however, are too large to confidently make inferences on its interior.

55 Cancri e and the planets in the Kepler-60 system are also lighter than the lightest rocky planets considered here (Fig. 7). This observation implies that such low-mass planets have thick atmospheres, which increase their radii by significant amounts as suggested by, e.g., Fortney et al. (2007). However, the presence of large amounts of lighter material such as water, ices or carbon compounds, not considered in this study, can also explain their low mean density, increasing the degeneracy (e.g., Seager et al., 2007; Valencia et al., 2007; Grasset et al., 2009).

## 6. Uncertainties on the interior structure of Kepler-36b

In this section we compute in detail the interior density, pressure and temperature profiles and the core radius fraction ($r_{CMB}$) for one example, Kepler-36b, a rocky super-Earth with the smallest uncertainty on its observed mass and radius, $M = 4.45^{+0.33}_{-0.27}$ $M_\oplus$ and $R = 1.486 \pm 0.035$ $R_\oplus$ (Carter et al., 2012). Assuming a pure Fe core and an $MgSiO_3$ mantle and using the SEOS for Fe, $r_{CMB}$ of Kepler-36b is $0.527^{+0.018}_{-0.012}$, implying it is an Earth-like planet by our definition (Fig. 8(d)). Use of equations of state of Fe other than SEOS changes $r_{CMB}$ by $-1$% to 4% (see Fig. F.12). The associated relative differences in density and pressure profiles reach 15%. Density increases monotonically from the surface to the center due to adiabatic self-compression, with discontinuous jumps at the mantle phase transitions, dominated by the perovskite and ppv forming transitions. Phases beyond ppv (Umemoto and Wentzcovitch, 2011) do not occur because the pressures in the mantle of Kepler-36b are not high enough for the dissociation.

A change of planetary temperature profiles has a small effect on the interior properties of Kepler-36b (Fig. 8d). Assuming an isothermal core with a CMB temperature jump of 9000 K, determined by the melting temperature of $MgSiO_3$ at 0.6 TPa (Belonoshko et al., 2005), increases $r_{CMB}$ by 1% (Fig. 8(d)). A super-adiabatic thermal gradient in the lower mantle further increases $r_{CMB}$ by 2%. Core densities and pressures decrease by up to 2% because of a hotter and lighter interior. Since the super-adiabatic temperatures are below the solvus temperature of MgO (Wahl and Militzer, 2015), we do not expect high-temperature miscibility of iron and rock in the interior of Kepler-36b.

The presence of light elements in the core has a significant effect on the interior properties of Kepler-36b. Considering core compositions of 0.9$\rho$ Fe and 0.8$\rho$ Fe (equivalent to FeS), we predict $r_{CMB}$ of Kepler-36b to increase by 9% and 22% compared to the case of pure Fe. The central density and pressure decrease by $\sim$13% ($\sim$25%) for 0.9$\rho$ Fe (0.8$\rho$ Fe). The combination of a $MgSiO_3$ mantle and a 0.8$\rho$ Fe core yields the largest core for Kepler-36b within our model scenarios.

Using different MgO-$SiO_2$-based mantle compositions ($Mg_2SiO_4$ and $SiO_2$) show small effects on the core radius (1% and-2%, respectively). Switching to FeO-based end-members, i.e., $FeSiO_3$ and $Fe_2SiO_4$, the interior of Kepler-36b cannot be modeled successfully, because resulting densities are so high that the resulting mass exceeds the measured value for Kepler-36b. For instance, a pure $FeSiO_3$ planet with no core and a radius of 1.486 $R_\oplus$ would have a mass of 4.7 $M_\oplus$ which exceeds the mass of Kepler-36b by 6%.

With a mid-member mantle composition of $Mg_{0.5}Fe_{0.5}SiO_3$ we find $r_{CMB} = 0.330^{+0.045}_{-0.036}$, which is smaller than the case of $MgSiO_3$ by 37%. In the core, the density, pressure and temperature decrease by as much as 25%, while in the mantle there is a significant increase only in density, but not pressure or temperature (Fig. 8). Theoretically, the mass of Kepler-36b can be explained without

[2] http://exoplanetarchive.ipac.caltech.edu .

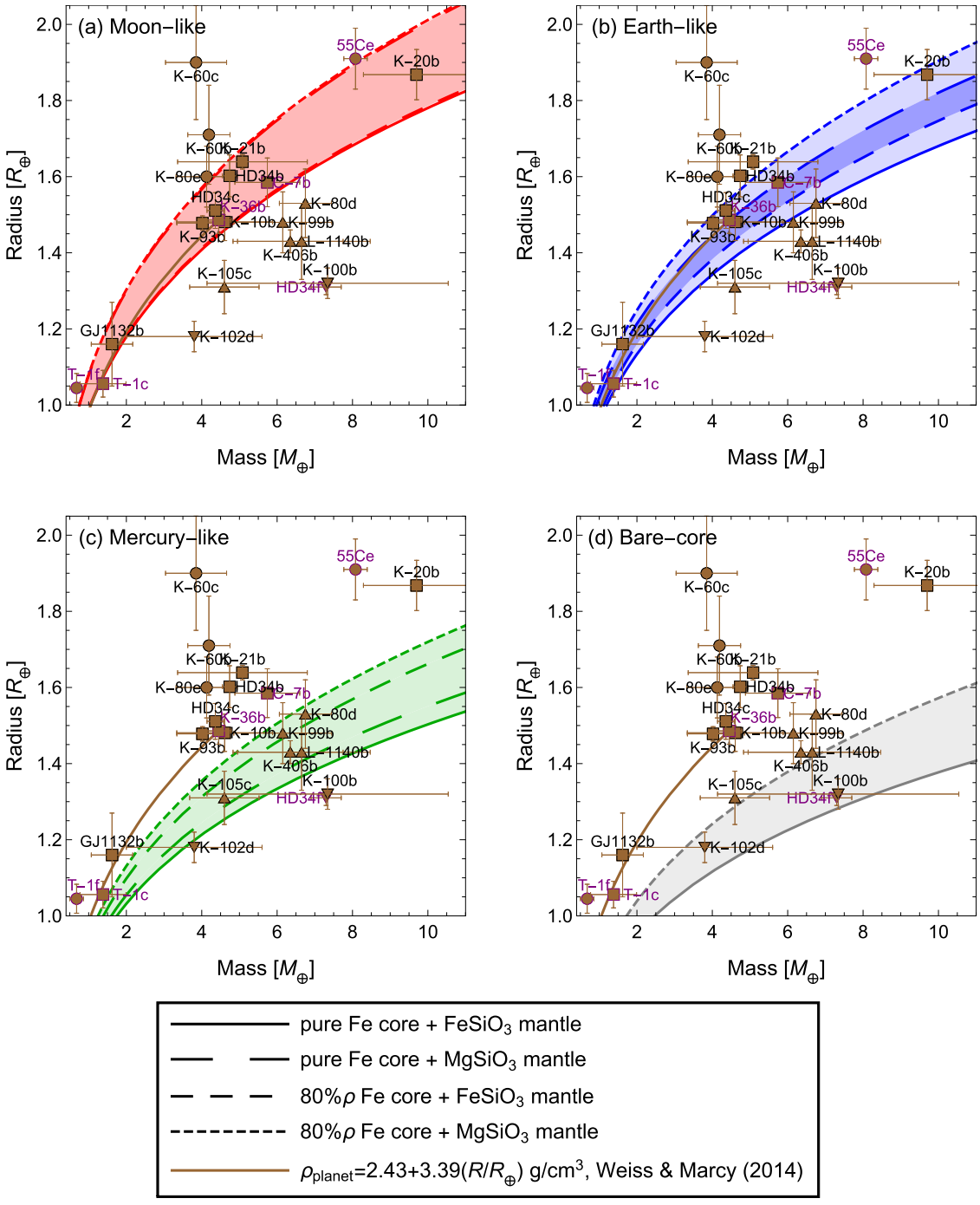


**Fig. 7.** $M-R$ relations of bare-core, Mercury-, Earth- and Moon-like super-Earths with fixed core radius fractions. Core compositions are 0.8$\rho$ Fe or pure Fe and mantle compositions of $MgSiO_3$ or $FeSiO_3$, although $FeSiO_3$ is much less likely. Observed exoplanets shown as squares have core radius fraction similar to the Earth or smaller, triangles have core radius fraction much larger than the Earth, inverted triangles have almost naked cores and circles are likely composed of significant amounts of volatile material or gas envelopes. Planets highlighted in violet are discussed in the text. Notation: T: TRAPPIST, K: Kepler, C: CoRoT, 55Ce: 55 Cnc e, HD34: HD 219134, L: LHS. (For interpretation of the references to color in this figure legend, the reader is referred to the web version of this article.)

any core, by considering an undifferentiated composition of about $Mg_{0.15}Fe_{0.85}SiO_3$.

Taking all observational and modeling uncertainties into account, it is possible to give an upper bound to the core radius of Kepler-36b of $r_{CMB} = 0.67$. For the models considered here with both the core and mantle, the central density and the central pressure belong in the range 16.3–22.9 Mg/m$^3$ and 1.4-2.2 TPa. For our coreless model, the central density and the central pressure are 11.2 Mg/m$^3$ and 1.0 TPa. The differences in the interior properties of Kepler-36b due to modeling uncertainties illustrate that temperature and equation of state of iron play a minor role on planetary interiors, compared to composition. As Fig. 8 clearly demonstrates, modeling uncertainties dominate over observational uncertainties on the interior properties of Kepler-36b.

## 7. Summary and conclusions

Previous studies (e.g., Seager et al., 2007; Grasset et al., 2009; Wagner et al., 2011) have pointed to the uncertainty of the equations of state of iron at pressures relevant to super-Earth cores (above 0.3 TPa) due to a lack of experimental data. In this paper,

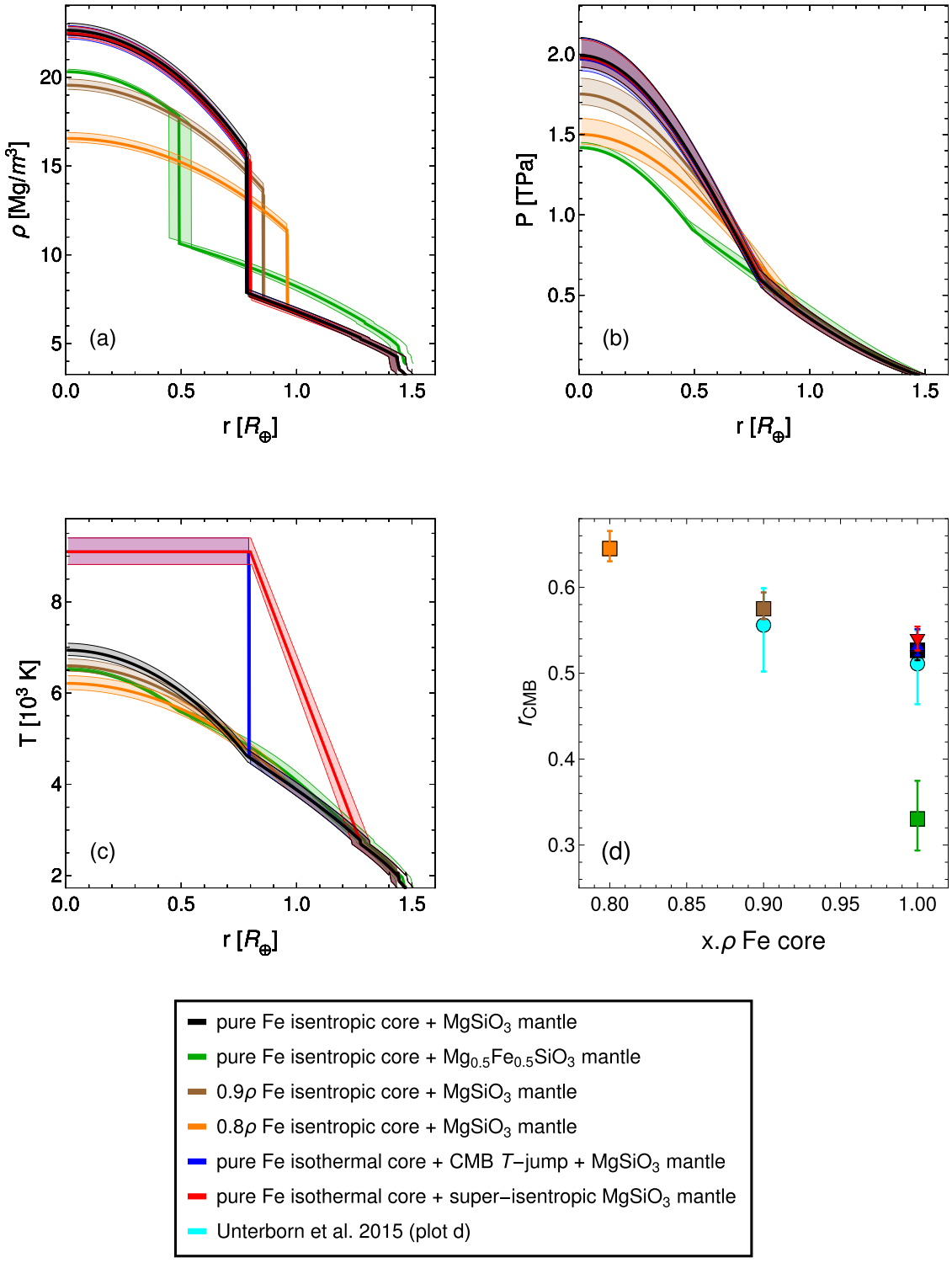


**Fig. 8.** Density, pressure and temperature distribution, and the core radius fraction of Kepler-36b for selected modeling scenarios. Shaded areas represent uncertainties arising due to uncertainties in mass and radius of Kepler-36b. (For interpretation of the references to color in this figure legend, the reader is referred to the web version of this article.)

we derive a new ab initio equation of state of iron for super-Earths (SEOS) based on Density Functional Theory (DFT) calculations. In addition to the discrete set of ab initio results given in the supplement, we also provide a closed equation of state expression by fitting the DFT results to the Holzapfel equation to 10 TPa.

Density differences between SEOS and other equations of state of iron from the literature are restricted to $\pm 2\%$ up to $\sim 0.5$ TPa, but range between-20% and 5% at 10 TPa. The equation of state from Bouchet et al. (2013) based on the Holzapfel formulation has the smallest density difference with SEOS ($<3.5\%$) up to 10 TPa. These density differences have significant effects on mass-radius relations of rocky super-Earths without gaseous envelopes, in particular for planets with an iron-core large enough to reach pressures where extrapolations of equations of state of iron are required. For models with an Earth-like core radius fraction of 0.5, the use of an inadequate equation of state can result in a differ-

ence in the mass of up to 10% for a 2 $R_\oplus$ super-Earth, and a difference in the radius of up to 3% for a 10 $M_\oplus$ super-Earth. For models with Mercury-like core radius fraction of 0.8 and bare-core models, these effects are even larger, reaching 20% in mass and 6% in radius. For models with Moon-like core radius fraction of 0.2, the core pressures are not high enough to induce significant differences in mass-radius relations.

Although the effects of temperature on mass-radius relations are smaller than those of the equation of state for iron, assumptions of an extreme CMB temperature jump or a super-adiabatic temperature profile in the lower mantle can change the mass of super-Earths by up to 5%, depending on the core size. We find that mantle temperatures, when assuming a super-adiabatic profile, are too low to allow for rock and iron to mix for planets smaller than 1.75 $R_\oplus$. Light elements in the core can strongly reduce the density in the core and therefore the mass of an exoplanet. By assuming a FeS core (equivalent to a reduction in density with respect to iron of 20%) instead of pure Fe, mass decreases by up to 13% and 33% for Earth- and Mercury-like super-Earths, respectively. The impact of the Mg/Si ratio on the mass-radius relations is very small because of the similarity in densities of MgO-$SiO_2$-based minerals. However, the presence of FeO in the mantle has a significant effect, as Fe-bearing minerals have higher densities than Mg-bearing minerals. Assuming a mantle composition of pure $FeSiO_3$, although much less likely than $MgSiO_3$, for a fixed mass, decreases the radius by up to 8% and 10% for Earth- and Moon-like super-Earths, respectively.

To quantify the effects of modeling uncertainties on the interior structure, we use Kepler-36b, a super-Earth with well-constrained mass and radius, as a test case. We demonstrate that the uncertainties due to the equation of state of iron (5%), temperature (2%), core and mantle composition (>20%) on the core radius of Kepler-36b dominate over the observational uncertainties on its mass and radius, which are 7% and 2%, respectively. Similar modeling uncertainties are observed for other interior properties such as central density and pressure.

We show that the use of an appropriate equation of state of iron (Appendix A) reduces the degeneracy in interpretations of mass and radius, but that uncertainties in composition, and to a minor extent temperature, lead to a spread of mass-radius curves into bands for Moon-, Earth- and Mercury-like exoplanets that can overlap. This significantly limits the ability to accurately infer the interior structure of rocky super-Earths. For example, the mass and radius of CoRoT-7b can equally be satisfied by a pure Fe core and a $MgSiO_3$ mantle for an Earth-like core or a pure Fe core and a $FeSiO_3$ mantle for a Moon-like core. This non-uniqueness adds to the large degeneracy that may result from not knowing if the planet has a substantial gaseous envelope. Since masses and radii of rocky super-Earths are expected to be determined with an accuracy as high as 3% in the planet radius and 10% in the planet mass (Hatzes et al., 2016) with upcoming missions such as TESS, CHEOPS, JWST and PLATO, modeling uncertainties will then dominate over observational uncertainties. Knowledge of the stellar composition, for example Fe/Si and Mg/Si ratios, would play an important role in mitigating the *M-R* degeneracy (Dorn et al., 2015; Santos et al., 2017).

## Acknowledgments

We thank Diana Valencia and an anonymous reviewer for their insightful comments in improving this manuscript. This research has been supported by the Planetary and Exoplanetary Science Network (PEPSci), funded by the Netherlands Organization for Scientific Research (NWO) Project no. 648.001.005, led by Carsten Dominik and Wim van Westrenen. TVH and AR acknowledge the financial support from the Belgian PRODEX program (grant no. 4000120791) managed by the European Space Agency in collaboration with the Belgian Federal Science Policy Office and from the BRAIN-be program of the Belgian Federal Science Policy Office. SC acknowledges financial support from OCAS NV by an OCAS-endowed chair at Ghent University. Work by GSN is supported by Deutsche Forschungsgemeinschaft (DFG, German Science Foundation) through Research Unit 2440 (Matter Under Planetary Interior Conditions, STE1105/13-1).

## Appendix A. Equation of state extrapolations

In order to assess which equation of state among the third-order Birch–Murnaghan (BM3), Vinet, modified Rydberg, and Holzapfel is more suitable for extrapolation, we fit them to the low pressure part (0–300 GPa) of our DFT calculated $P(V)$ set (Appendix G) and compare the pressures predicted with our set of results (up to 10 TPa). For all equations, every parameter has been estimated without any prior constraints except for the modified Rydberg equation where $K'_\infty > 5/3$ has been assumed.

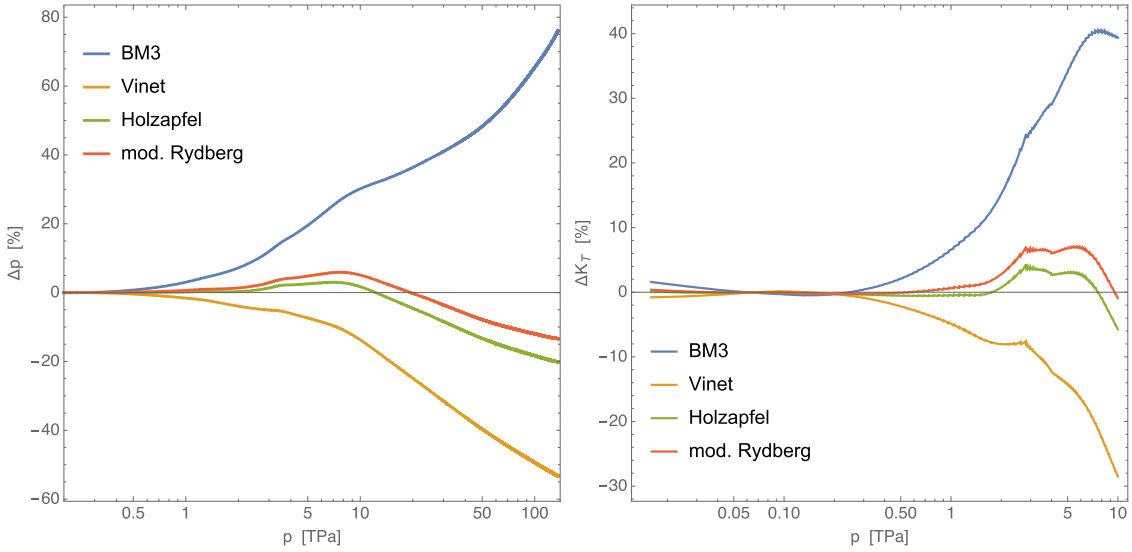


**Fig. A.9.** Relative differences in $P$ and $K_T$ between the DFT results and predictions obtained with the BM3, Vinet, modified Rydberg, and Holzapfel equation as a function of pressure. (For interpretation of the references to color in this figure legend, the reader is referred to the web version of this article.)

The BM3 and Vinet equations have residuals below 0.4 GPa and those of the modified Rydberg and Holzapfel are below 0.05 GPa. This is significantly smaller than present day experimental error (< 2%) (Fei et al., 2016). Consequently, they are equally suitable for summarizing the low pressure data. Note that an unconstrained fit with the modified Rydberg equation has smaller residuals than the constrained fit, but the estimated value of $K'_\infty$ is 1.43, smaller than the theoretical value of 5/3 (Stacey, 2005).

Extrapolation with the Vinet and BM3 equation results in differences that are already above 2% at pressures that are not much larger than 1 TPa and above 14% at 10 TPa (Fig. A.9). The pressures predicted by the modified Rydberg and Holzapfel equations differ significantly less from the DFT results (Fig. A.9). Up to 10 TPa the difference are below 3% for the modified Rydberg (not shown) and Holzapfel equations. Differences with the "constrained" modified Rydberg are about two times larger. Note that at 137 TPa the predicted pressures with the BM3 and Vinet equation differ from the DFT set by more than 50% and the modified Rydberg and Holzapfel equation by about 20%. For completeness we also compare $K_T$ predicted by the equations of state and directly calculated from the DFT set (Fig. A.9).

## Appendix B. Fitting residuals of DFT data

Fig. B.10 demonstrates that the whole DFT result set (Appendix G) cannot be summarized accurately with one equation of state. However, a fit on a subset (0.234–10 TPa) with the Holzapfel equation has residuals that are below 2% if the reference volume is given (see main text). Comparable residuals are obtained for data at $P < 5$ TPa.

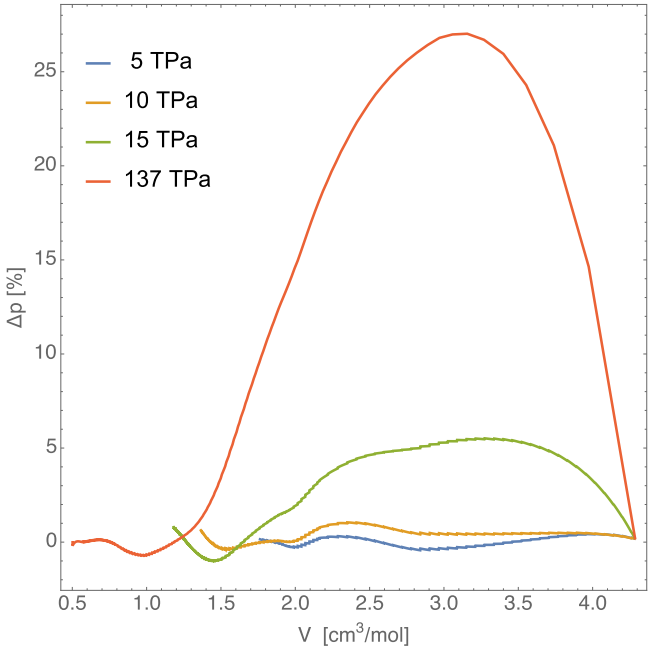


**Fig. B.10.** Fit residuals of the Holzapfel equation for different subsets of the DFT results. (For interpretation of the references to color in this figure legend, the reader is referred to the web version of this article.)

## Appendix C. Sliding window interpolation scheme

To compute volumes at intermediate pressures we use a sliding-window local third-order Birch–Murnaghan (BM3) fitting scheme. Let $\{V_i,\ E_i,\ P_i\}_{1 \le i \le N}$ be the volume, energy, and pressure data set. The volume and bulk modulus at pressure $\tilde{P}$ is then calculated as follows:

1. Locate the position of the pressure in $\{P_i\}_{1 \le i \le N}$ that is closest to $\tilde{P}$, say at $k$,
2. select a small subset of length $2l + 1$ of volumes and internal energies around $P_k$: $\{V_j, E_j\}_{k-l \le j \le k+l}$,
3. define a local enthalpy as: $H(V) = E(V) + \tilde{P}\,V$ (per construction $H$ has a minima at $P = \tilde{P}$, since $\frac{dE}{dV} = -P$),
4. estimate $V$ and $K_T$ at $\tilde{P}$ by fitting the BM3 equation on $\{V_j, H_j\}_{k-l \le j \le k+l}$.

This scheme can be used to compute $V$ and $K_T$ on the fly or beforehand. In practice, the size of the local subset is chosen large enough to allow for a precise fit but not much larger. We have used $l = 7$.

## Appendix D. Equation of state of iron-alloys

Sata et al. (2010) determined the density of FeS, FeSi, $Fe_{0.95}O$ and $Fe_3C$ experimentally in a pressure range relevant for the Earth's core and fitted the data to a BM3 equation. In the absence of data in the high-pressure range of the super-Earth cores, extrapolations significantly beyond the experimental pressure range are needed. Such extrapolations can result in unreasonably large deviations (see Fig. 2). Since extrapolation with a Holzapfel equation leads to better results than with a BM3 equation (Fig. B.10), we have refitted the density data from Sata et al. (2010) to a Holzapfel equation (Table D.5).

**Table D.5**
Thermoelastic parameters obtained by fitting the data of FeS, FeSi, $Fe_{0.95}O$ and $Fe_3C$ from Sata et al. (2010) to a Holzapfel equation.

| Fe-alloy | $\rho_0$ ($\frac{kg}{m^3}$) | $K_{T,0}$ (GPa) | $K'_{T,0}$ | $P_{FG0}$ (TPa) |
|---|---|---|---|---|
| FeS | 6118 | 144.3 | 4.79 | 27.78 |
| FeSi | 6522 | 219.5 | 4.29 | 18.45 |
| $Fe_{0.95}O$ | 5764 | 152.7 | 4.13 | 11.25 |
| $Fe_3C$ | 7980 | 289.4 | 3.81 | 30.68 |

Key: $\rho_0$: reference density at $P_0 = 1$ bar and $T_0 = 300$ K, $K_{T,0}$: reference isothermal bulk modulus and its derivative $K'_{T,0}$, $P_{FG0}$: Fermi-gas pressure.

## Appendix E. DFT equations of state of iron

In Fig. E.11, we compare our DFT results at low pressures (0–300 GPa) with similar DFT predictions and laboratory data from the literature. We compare our DFT results at zero pressure with studies from the literature in Table E.6.

**Table E.6**
Ab initio equations of state of hcp-Fe.

| $V_0$ ($cm^3$/mol) | $K_0$ (GPa) | $K'_0$ | XC | Reference |
|---|---|---|---|---|
| 6.145 | 291 | 4.4 | PW91 | Stixrude et al. (1994), NM |
| 6.136-6.250 | 287–296 | 4.2–4.5 | PW91 | Alfè et al. (2000), NM |
| 6.175 | 293 | – | PW91 | Caspersen et al. (2004), NM |
| 6.158 | 292 | 4.4 | PBE | Steinle-Neumann et al. (1999), NM |
| 6.078 | 296 | – | PBE | Sha and Cohen (2010), NM |
| 6.135 | 291 | 5.1 | PBE | This Work, NM |
| 6.315 | 224 | 5.5 | PBE | Dewaele et al. (2006), AFM |
| 6.354 | 209 | 5.2 | PBE | Steinle-Neumann et al. (1999), AFM |
| 6.306 | 222 | 5.7 | PBE | This Work, AFM |

Key: XC: Exchange correlation functional of hcp-Fe, NM: non-magnetic, AFM: antiferromagnetic, PW91: Perdew and Wang (1992), PBE: Perdew et al. (1996). Reference temperature and pressure are zero.

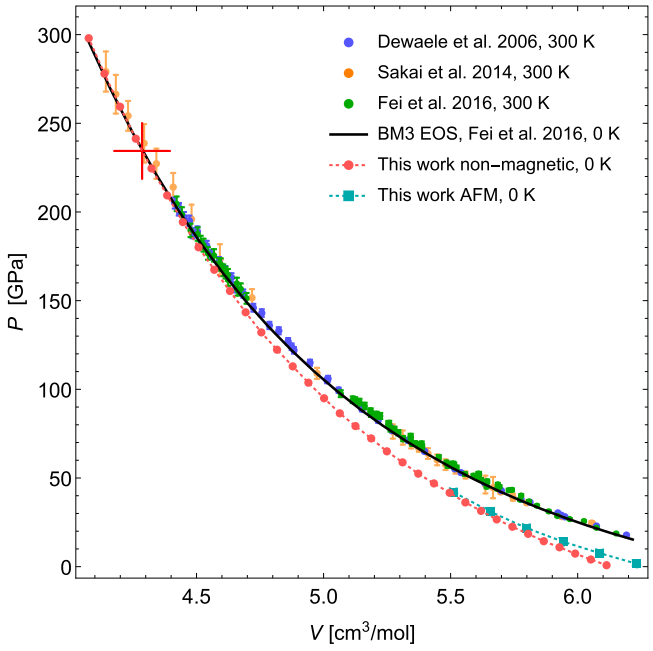


**Fig. E.11.** Pressure of hcp iron as a function of volume. Recent laboratory data with error-bars, DFT results for non-magnetic and anti-ferromagnetic phases, and the BM3 equation of state from Fei et al. (2016) corrected to 0 K and zero-point vibrational effects (Lejaeghere et al., 2014). The red plus denotes the pressure (234.4 GPa) and volume (4.28575 $cm^3$/mol) at which our DFT results match the experimental equation of state from Fei et al. (2016). (For interpretation of the references to color in this figure legend, the reader is referred to the web version of this article.)

## Appendix F. Equations of state of iron and effects on Kepler-36b

Table F.7 lists the thermoelastic parameters of various equations of state of iron from the literature used for modeling planetary cores. In Fig. F.12, we illustrate the differences between our DFT-based equation of state and some equations of state from Table F.7 on the internal properties of Kepler-36b.

**Table F.7**
Thermoelastic parameters for various equations of state of iron from the literature.

| Ref. | Form. | Isothermal | | | | Harmonic | | | | Anharmonic + Electronic | | | | |
|---|---|---|---|---|---|---|---|---|---|---|---|---|---|---|
| | | $\rho_0$ ($\frac{kg}{m^3}$) | $K_{T,0}$ (GPa) | $K'_{T,0}$ | $K'_{T,\infty}$ | $\Theta_0$ (K) | $\gamma_0$ | $b$ [$q$] | $\gamma_\infty$ | $a_0$ ($\frac{1}{10^3\ K}$) | $m$ | $e_0$ ($\frac{1}{10^3\ K}$) | $g$ | $P$ range (GPa) |
| Dew | Vin | 8270 | 163.4 | 5.38 | – | 417 | 1.875 | 3.289 | 1.305 | 0.037 | 1.87 | 0.195 | 1.339 | 17–197 |
| Bou | Hol | 8878 | 253.8 | 4.719 | – | 44.574 | 1.408 | 0.826 | 0.827 | 0.2121 | 1.891 | – | – | 30–1500 |
| Val | Vin | 8300 | 160.2 | 5.82 | – | 998 | 1.36 | [0.91] | – | – | – | – | – | 136–300 |
| Sea | Vin | 8300 | 156.2 | 6.08 | – | – | – | – | – | – | – | – | – | 0–330 |
| Fei | BM3 | 8269 | 172.7 | 4.79 | – | 422 | 1.74 | [0.78] | – | – | – | – | – | 18–280 |
| Dor | BM3 | 8341 | 173.98 | 5.297 | – | – | 2.434 | [0.489] | – | – | – | – | – | 18–360 |
| Wag | Ryd | 8269 | 149.4 | 5.65 | 2.94 | 430 | 1.875 | 3.289 | 1.305 | 0.037 | 1.87 | 0.195 | 1.339 | 17–197 |

Key: $\rho_0$: reference density at ambient conditions, $K_0$: reference isothermal bulk modulus and its derivatives $K'_{T,0}$ and $K'_{T,\infty}$. Note: Fei et al. (2016) uses a different formulation for the electronic contribution to the specific heat, $C_{Ve} = \beta_0 x^{3k} T$, where $\beta_0 = 0.07$ J kg$^{-1}$ K$^{-2}$ and $k = 1.34$, and $\gamma_e = 2$.
Abbreviations: Dew: Dewaele et al. (2006); Bou: Bouchet et al. (2013); Val: Valencia et al. (2007), data from Williams and Knittle (1997); Sea: Seager et al. (2007), data from Anderson et al. (2001); Fei: Fei et al. (2016); Dor: Dorn et al. (2015), data from Belonoshko et al. (2010); Wagner et al. (2011), data from Dewaele et al. (2006); Vin: Vinet; BM3: third-order Birch-Murnaghan; Hol: Holzapfel; Ryd: modified Rydberg.

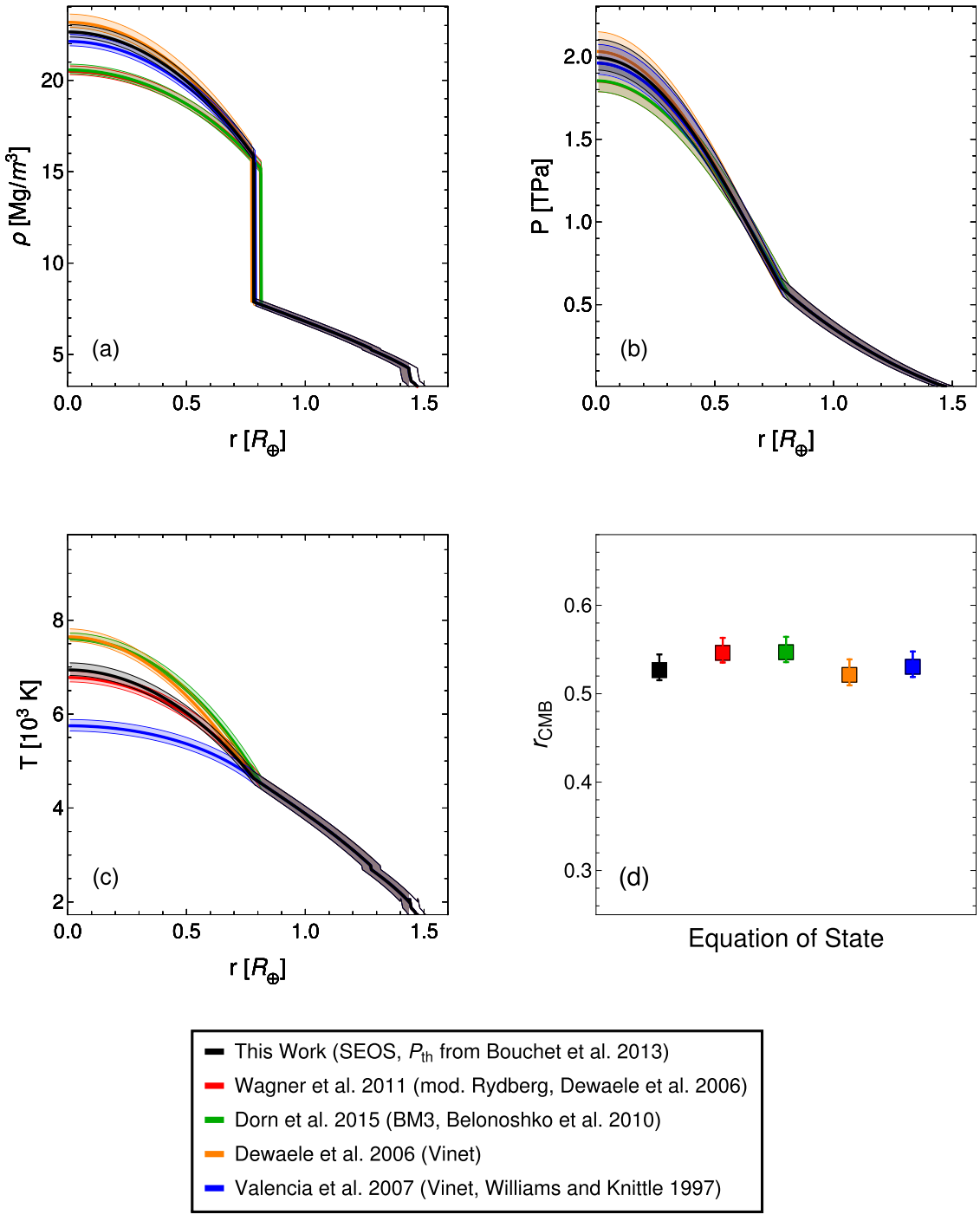


**Fig. F.12.** Density, pressure and temperature distribution, and the core radius fraction of Kepler-36b calculated using different equations of state of iron. Shaded areas represent uncertainties arising due to uncertainties in mass and radius of Kepler-36b. (For interpretation of the references to color in this figure legend, the reader is referred to the web version of this article.)

## Supplementary material

Supplementary material associated with this article can be found, in the online version, at 10.1016/j.icarus.2018.05.005.

## References

Alfè, D., Gillan, M.J., Price, G.D., 2002. Composition and temperature of the Earth's core constrained by combining ab initio calculations and seismic data. Earth Planet. Sci. Lett. 195, 91–98. doi:10.1016/S0012-821X(01)00568-4.

Alfè, D., Kresse, G., Gillan, M.J., 2000. Structure and dynamics of liquid iron under Earth's core conditions. Phys. Rev. B 61, 132–142. cond-mat/9905319 doi: 10.1103/PhysRevB.61.132.

Alfè, D., Price, G.D., Gillan, M.J., 2002. Iron under Earth's core conditions: liquid-state thermodynamics and high-pressure melting curve from ab initio calculations. Phys. Rev. B 65, 165118. doi:10.1103/PhysRevB.65.165118.

Anderson, O.L., Dubrovinsky, L., Saxena, S.K., LeBihan, T., 2001. Experimental vibrational Grüneisen ratio values for $\epsilon$-iron up to 330 GPa at 300 K. Geophys. Res. Lett. 28, 399–402. doi:10.1029/2000GL008544.

Atkins, P.W., 1994. Physical Chemistry. W.H. Freeman.

Batalha, N.M., et al., 2011. Kepler's first rocky planet: Kepler-10b. Astrophys. J. 729, 27. 1102.0605 doi: 10.1088/0004-637X/729/1/27.

Belonoshko, A.B., Bryk, T., Rosengren, A., 2010. Shear relaxation in iron under the conditions of Earth's inner core. Phys. Rev. Lett. 104 (24), 245703. doi:10.1103/PhysRevLett.104.245703.

Belonoshko, A.B., Lukinov, T., Fu, J., Zhao, J., Davis, S., Simak, S.I., 2017. Stabilization of body-centred cubic iron under inner-core conditions. Nat. Geosci. 10, 312–316. doi:10.1038/ngeo2892.

Belonoshko, A.B., et al., 2005. High-Pressure melting of $MgSiO_3$. Phys. Rev. Lett. 94 (19), 195701. doi:10.1103/PhysRevLett.94.195701.

Bond, J.C., O'Brien, D.P., Lauretta, D.S., 2010. The compositional diversity of extrasolar terrestrial planets. i. in situ simulations. Astrophys. J. 715, 1050–1070. 1004.0971 doi: 10.1088/0004-637X/715/2/1050.

Borucki, W.J., et al., 2011. Characteristics of Kepler planetary candidates based on the first data set. Astrophys. J. 728, 117. doi:10.1088/0004-637X/728/2/117.

Bouchet, J., Mazevet, S., Morard, G., Guyot, F., Musella, R., 2013. Ab initio equation of state of iron up to 1500 GPa. Phys. Rev. B 87 (9), 094102. doi:10.1103/PhysRevB.87.094102.

Buchhave, L.A., et al., 2014. Three regimes of extrasolar planet radius inferred from host star metallicities. Nature 509, 593–595. 1405.7695 doi: 10.1038/nature13254.

Carter, J.A., et al., 2012. Kepler-36: a pair of planets with neighboring orbits and dissimilar densities. Science 337. 556–. 1206.4718 doi: 10.1126/science.1223269.

Carter-Bond, J.C., O'Brien, D.P., Delgado Mena, E., Israelian, G., Santos, N.C., González Hernández, J.I., 2012a. Low MgSi planetary host stars and their Mg-depleted terrestrial planets. Astrophys. J. Lett. 747, L2. 1201.1939 doi: 10.1088/2041-8205/747/1/L2.

Carter-Bond, J.C., O'Brien, D.P., Raymond, S.N., 2012b. The compositional diversity of extrasolar terrestrial planets. II. migration simulations. Astrophys. J. 760, 44. 1209.5125 doi: 10.1088/0004-637X/760/1/44.

Caspersen, K.J., Lew, A., Ortiz, M., Carter, E.A., 2004. Importance of shear in the bcc-to-hcp transformation in iron. Phys. Rev. Lett. 93 (11), 115501. doi:10.1103/PhysRevLett.93.115501.

Cebulla, D., Redmer, R., 2014. Ab initio simulations of MgO under extreme conditions. Phys. Rev. B 89 (13), 134107. doi:10.1103/PhysRevB.89.134107.

Chust, T.C., Steinle-Neumann, G., Dolejš, D., Schuberth, B.S.A., Bunge, H.-P., 2017. Mma-eos: a computational framework for mineralogical thermodynamics. J. Geophys. Res. 122 (12), n/a–n/a. 2017JB014501 doi: 10.1002/2017JB014501.

Connolly, J.A.D., Khan, A., 2016. Uncertainty of mantle geophysical properties computed from phase equilibrium models. Geophys. Res. Lett. 43 (10), 5026–5034. doi:10.1002/2016GL068239.

Cottenier, S., 2002. Density Functional Theory and the family of (L)APW-methods: a step-by-step introduction. Instituut voor Kern- en Stralingsfysica, K.U.Leuven, Belgium.

Cottenier, S., Probert, M., Van Hoolst, T., Van Speybroeck, V., Waroquier, M., 2011. Crystal structure prediction for iron as inner core material in heavy terrestrial planets. Earth Planet. Sci. Lett. 312 (1–2), 237–242.

Dewaele, A., Loubeyre, P., Occelli, F., Mezouar, M., Dorogokupets, P.I., Torrent, M., 2006. Quasihydrostatic equation of state of iron above 2 Mbar. Phys. Rev. Lett. 97, 215504. doi:10.1103/PhysRevLett.97.215504.

Dorn, C., et al., 2015. Can we constrain the interior structure of rocky exoplanets from mass and radius measurements? Astronom. Astrophys. 577, A83. 1502.03605 doi: 10.1051/0004-6361/201424915.

Dubrovinksy, 2007. Body-centered cubic iron-nickel alloy in Earth's core. Science 316, 5833. doi:10.1126/science.1142105. http://www.sciencemag.org/content/316/5833/1880.full

Dziewonski, A.M., Anderson, D.L., 1981. Preliminary reference earth model. Phys. Earth Planet. Inter. 25 (4), 297–356. doi:10.1016/0031-9201(81)90046-7.

Fei, Y., Brosh, E., 2014. Experimental study and thermodynamic calculations of phase relations in the Fe-C system at high pressure. Earth Planet. Sci. Lett. 408, 155–162. doi:10.1016/j.epsl.2014.09.044.

Fei, Y., Murphy, C., Shibazaki, Y., Shahar, A., Huang, H., 2016. Thermal equation of state of hcp-iron: constraint on the density deficit of Earth's solid inner core. Geophys. Res. Lett. 43, 6837–6843. doi:10.1002/2016GL069456.

Fortney, J.J., Marley, M.S., Barnes, J.W., 2007. Planetary radii across five orders of magnitude in mass and stellar insolation: application to transits. Astrophys. J. 659, 1661–1672. astro-ph/0612671 doi: 10.1086/512120.

Fulton, B.J., et al., 2017. The California-Kepler survey. III. a gap in the radius distribution of small planets. Astron. J. 154, 109. 1703.10375 doi: 10.3847/1538-3881/aa80eb.

Garcia, R.F., Gagnepain-Beyneix, J., Chevrot, S., Lognonné, P., 2011. Very preliminary reference moon model. Phys. Earth Planet. Inter. 188, 96–113. doi:10.1016/j.pepi.2011.06.015.

Grasset, O., Schneider, J., Sotin, C., 2009. A study of the accuracy of mass-radius relationships for silicate-rich and ice-rich planets up to 100 Earth masses. Astrophys. J. 693 (1), 722.

Hatzes, A.P., Weiss, W.W., Rauer, H., Grotsch-Noels, A., 2016. V.3 Present and future space missions for ultra-precision photometry, p. 241. doi:10.1051/978-2-7598-1876-1.c053.

Hauck, S.A., et al., 2013. The curious case of Mercury's internal structure. J. Geophys. Res. 118 (6), 1204–1220. doi:10.1002/jgre.20091.

Hirose, K., Labrosse, S., Hernlund, J., 2013. Composition and state of the core. Annu. Rev. Earth Planet. Sci. 41, 657–691. doi:10.1146/annurev-earth-050212-124007.

Holzapfel, W.B., 1996. Physics of solids under strong compression. Rep. Prog. Phys. 59, 29–90. doi:10.1088/0034-4885/59/1/002.

Ichikawa, H., Tsuchiya, T., Tange, Y., 2014. The p-v-t equation of state and thermodynamic properties of liquid iron. J. Geophys. Res. 119 (1), 240–252. 2013JB010732 doi: 10.1002/2013JB010732.

Javoy, M., et al., 2010. The chemical composition of the earth: enstatite chondrite models. Earth Planet. Sci. Lett. 293 (3–4), 259–268. doi:10.1016/j.epsl.2010.02.033.

Laio, A., Bernard, S., Chiarotti, G.L., Scandolo, S., Tosatti, E., 2000. Physics of iron at Earth's core conditions. Science 287, 1027–1030. doi:10.1126/science.287.5455.1027.

Léger, A., et al., 2009. Transiting exoplanets from the CoRoT space mission. VIII. CoRoT-7b: the first super-Earth with measured radius. AAP 506, 287–302. 0908.0241 doi: 10.1051/0004-6361/200911933.

Lejaeghere, K., et al., 2016a. Reproducibility in density functional theory calculations of solids. Science 351. doi:10.1126/science.aad3000.

Lejaeghere, K., Cottenier, S., Van Speybroeck, V., 2013. Ranking the stars: a refined pareto approach to computational materials design. Phys. Rev. Lett. 111 (7), 075501. doi:10.1103/PhysRevLett.111.075501.

Lejaeghere, K., Jaeken, J., Van Speybroeck, V., Cottenier, S., 2014. Ab initio based thermal property predictions at a low cost: an error analysis. Phys. Rev. B 89 (1), 014304. doi:10.1103/PhysRevB.89.014304.

Lejaeghere, K., Vanduyfhuys, L., Verstraelen, T., Van Speybroeck, V., Cottenier, S., 2016b. Is the error on first-principles volume predictions absolute or relative? Comput. Mater. Sci 117, 390–396. doi:10.1016/j.commatsci.2016.01.039.

Madsen, G.K.H., Blaha, P., Schwarz, K., Sjöstedt, E., Nordström, L., 2001. Efficient linearization of the augmented plane-wave method. Phys. Rev. B 64 (19), 195134. doi:10.1103/PhysRevB.64.195134.

Mocquet, A., Grasset, O., Sotin, C., 2014. Very high-density planets: a possible remnant of gas giants. Philos. Trans. R. Soc. Lond. Series A 372. 20130164–20130164 doi: 10.1098/rsta.2013.0164.

Morard, G., Bouchet, J., Valencia, D., Mazevet, S., Guyot, F., 2011. The melting curve of iron at extreme pressures: implications for planetary cores. High Energy Density Phys. 7, 141–144. doi:10.1016/j.hedp.2011.02.001.

Perdew, J.P., Burke, K., Ernzerhof, M., 1996. Generalized gradient approximation made simple. Phys. Rev. Lett. 77, 3865–3868. doi:10.1103/PhysRevLett.77.3865.

Perdew, J.P., Wang, Y., 1992. Accurate and simple analytic representation of the electron-gas correlation energy. Phys. Rev. B 45, 13244–13249. doi:10.1103/PhysRevB.45.13244.

Pickard, C.J., Needs, R.J., 2009. Stable phases of iron at terapascal pressures. J. Phys.: Condens. Matter 21 (45), 452205.

Poirier, J.-P., 2000. Introduction to the Physics of the Earth's Interior (Cambridge Topics in Mineral Physics & Chemistry), 2 Cambridge University Press.

Pourovskii, L.V., Mravlje, J., Ferrero, M., Parcollet, O., Abrikosov, I.A., 2014. Impact of electronic correlations on the equation of state and transport in $\epsilon$-Fe. Phys. Rev. B 90 (15), 155120. 1312.3654 doi: 10.1103/PhysRevB.90.155120.

Rivoldini, A., Van Hoolst, T., 2013. The interior structure of Mercury constrained by the low-degree gravity field and the rotation of Mercury. Earth Planet. Sci. Lett. 377, 62–72. doi:10.1016/j.epsl.2013.07.021.

Rogers, L.A., 2015. Most 1.6 earth-radius planets are not rocky. Astrophys. J. 801, 41. 1407.4457 doi: 10.1088/0004-637X/801/1/41.

Sakai, T., Ohtani, E., Hirao, N., Ohishi, Y., 2011. Stability field of the hcp-structure for Fe, Fe-Ni, and Fe-Ni-Si alloys up to 3 Mbar. Geophys. Res. Lett. 38, L09302. doi:10.1029/2011GL047178.

Santos, N.C., et al., 2017. Constraining planet structure and composition from stellar chemistry: trends in different Stellar populations. Astronom. Astrophys. 608, A94. 1711.00777 doi: 10.1051/0004-6361/201731359.

Sata, N., Hirose, K., Shen, G., Nakajima, Y., Ohishi, Y., Hirao, N., 2010. Compression of FeSi, $Fe_3C$, $Fe_{0.95}O$, and FeS under the core pressures and implication for light element in the Earth's core. J. Geophys. Res. 115, B09204. doi:10.1029/2009JB006975.

Schaefer, L., Jacobsen, S.B., Remo, J.L., Petaev, M.I., Sasselov, D.D., 2017. Metal-silicate partitioning and its role in core formation and composition on super-Earths. Astrophys. J. 835, 234. doi:10.3847/1538-4357/835/2/234.

Schubert, G., Turcotte, D.L., Olson, P., 2001. Mantle convection in the earth and planets.

Schwarz, K., Blaha, P., Trickey, S.B., 2010. Electronic structure of solids with WIEN2k. Mol. Phys. 108, 3147–3166. doi:10.1080/00268976.2010.506451.

Seager, S., Kuchner, M., Hier-Majumder, C.A., Militzer, B., 2007. Mass-Radius relationships for solid exoplanets. Astrophys. J. 669, 1279–1297. 0707.2895 doi: 10.1086/521346.

Sha, X., Cohen, R.E., 2010. Elastic isotropy of $\varepsilon$-fe under Earth's core conditions. Geophys. Res. Lett. 37 (10). L10302 doi: 10.1029/2009GL042224.

Sjöstedt, E., Nordström, L., Singh, D.J., 2000. An alternative way of linearizing the augmented plane-wave method. Solid State Commun. 114, 15–20. doi:10.1016/S0038-1098(99)00577-3.

Sotin, C., Grasset, O., Mocquet, A., 2007. Mass radius curve for extrasolar earth-like planets and ocean planets. Icarus 191, 337–351. doi:10.1016/j.icarus.2007.04.006.

Stacey, F.D., 2005. High pressure equations of state and planetary interiors. Rep. Prog. Phys. 68 (2), 341.

Stamenković, V., Noack, L., Breuer, D., Spohn, T., 2012. The influence of pressure-dependent viscosity on the thermal evolution of super-Earths. Astrophys. J. 748, 41. doi:10.1088/0004-637X/748/1/41.

Steinle-Neumann, G., Stixrude, L., Cohen, R.E., 1999. First-principles elastic constants for the hcp transition metals Fe, Co, and Re at high pressure. Phys. Rev. B 60, 791–799. cond-mat/9904431 doi: 10.1103/PhysRevB.60.791.

Steinle-Neumann, G., Stixrude, L., Cohen, R.E., 2004. Magnetism in dense hexagonal iron. Proc. Natl. Acad. Sci. 101 (1), 33–36. doi:10.1073/pnas.2237239100. http://www.pnas.org/content/101/1/33.full.pdf

Stixrude, L., 2012. Structure of Iron to 1 Gbar and 40 000 K. Phys. Rev. Lett. 108 (5), 055505. doi:10.1103/PhysRevLett.108.055505.

Stixrude, L., 2014. Melting in super-Earths. Philos. Trans. R. Soc. Lond. Series A 372. doi:10.1098/rsta.2013.0076. 20130076–20130076

Stixrude, L., Cohen, R.E., Singh, D.J., 1994. Iron at high pressure: linearized-augmented-plane-wave computations in the generalized-gradient approximation. Phys. Rev. B 50, 6442–6445. doi:10.1103/PhysRevB.50.6442.

Stixrude, L., Lithgow-Bertelloni, C., 2011. Thermodynamics of mantle minerals - II. phase equilibria. Geophys. J. Int. 184, 1180–1213. doi:10.1111/j.1365-246X.2010.04890.x.

Tackley, P.J., Ammann, M., Brodholt, J.P., Dobson, D.P., Valencia, D., 2013. Mantle dynamics in super-Earths: post-perovskite rheology and self-regulation of viscosity. Icarus 225, 50–61. 1204.3539 doi: 10.1016/j.icarus.2013.03.013.

Tsuchiya, T., Tsuchiya, J., 2011. Prediction of a hexagonal $SiO_2$ phase affecting stabilities of $MgSiO_3$ and $CaSiO_3$ at multimegabar pressures. Proc. Natl. Acad. Sci. 108 (4), 1252–1255. doi:10.1073/pnas.1013594108. http://www.pnas.org/content/108/4/1252.full.pdf

Umemoto, K., Wentzcovitch, R.M., 2011. Two-stage dissociation in $MgSiO_3$ post-perovskite. Earth Planet. Sci. Lett. 311, 225–229. doi:10.1016/j.epsl.2011.09.032.

Unterborn, C.T., Dismukes, E.E., Panero, W.R., 2016. Scaling the Earth: A Sensitivity analysis of terrestrial exoplanetary interior models. Astrophys. J. 819, 32. 1510.07582 doi: 10.3847/0004-637X/819/1/32.

Valencia, D., O'Connell, R.J., Sasselov, D., 2006. Internal structure of massive terrestrial planets. Icarus 181, 545–554. astro-ph/0511150 doi: 10.1016/j.icarus.2005.11.021.

Valencia, D., Sasselov, D.D., O'Connell, R.J., 2007. Radius and structure models of the first super-Earth planet. Astrophys. J. 656, 545–551. astro-ph/0610122 doi: 10.1086/509800.

Vočadlo, L., Alfè, D., Gillan, M.J., Wood, I.G., Brodholt, J.P., Price, G.D., 2003. Possible thermal and chemical stabilization of body-centred-cubic iron in the Earth's core. Nature 424, 536–539. doi:10.1038/nature01829.

Vočadlo, L., et al., 2008. The stability of bcc-Fe at high pressures and temperatures with respect to tetragonal strain. Phys. Earth Planet. Inter. 170, 52–59. doi:10.1016/j.pepi.2008.07.032.

Wagner, F.W., Sohl, F., Hussmann, H., Grott, M., Rauer, H., 2011. Interior structure models of solid exoplanets using material laws in the infinite pressure limit. Icarus 214, 366–376. doi:10.1016/j.icarus.2011.05.027.

Wagner, F.W., Tosi, N., Sohl, F., Rauer, H., Spohn, T., 2012. Rocky super-Earth interiors. structure and internal dynamics of coroT-7b and kepler-10b. Astronom. Astrophys. 541, A103. doi:10.1051/0004-6361/201118441.

Wahl, S.M., Militzer, B., 2015. High-temperature miscibility of iron and rock during terrestrial planet formation. Earth Planet. Sci. Lett. 410, 25–33. 1608.01295 doi: 10.1016/j.epsl.2014.11.014.

Weiss, L.M., Marcy, G.W., 2014. The mass-radius relation for 65 exoplanets smaller than 4 Earth radii. Astrophys. J. Lett. 783, L6. 1312.0936 doi: 10.1088/2041-8205/783/1/L6.

Williams, Q., Knittle, E., 1997. Constraints on core chemistry from the pressure dependence of the bulk modulus. Phys. Earth Planet. Inter. 100, 49–59. doi:10.1016/S0031-9201(96)03231-1.

Wu, S.Q., et al., 2014. An adaptive genetic algorithm for crystal structure prediction. J. Phys.: Condens. Matter 26 (3), 035402.

Zapolsky, H.S., Salpeter, E.E., 1969. The mass-radius relation for cold spheres of low mass. Astrophys. J. 158, 809. doi:10.1086/150240.